Evolutionary rescue of spherical *mreB* deletion mutants of the rod-shape bacterium *Pseudomonas fluorescens* SBW25

P. Richard J. Yulo[⌘1], Nicolas Desprat[⌘2,3,4,¥], Monica L. Gerth[5,†], Barbara Ritzl-Rinkenberger[6,7], Andrew D. Farr[8], Yunhao Liu[5], Xue-Xian Zhang[1], Michael Miller[1], Felipe Cava[6,7], Paul B. Rainey[5,8,9,¥] & Heather L. Hendrickson[1,10,¥]

[1]Institute of Natural and Mathematical Science, Massey University, Auckland 0745, New Zealand. [2]Laboratoire de Physique de l'ENS, Ecole Normale Supérieure, PSL Research University; Université Paris-Cité; Sorbonne Universités; CNRS; 24 rue Lhomond, 75005 Paris, France. [3]Institut de biologie de l'Ecole normale supérieure (IBENS), Ecole normale supérieure, CNRS, INSERM, PSL Research University, 46 rue d'Ulm, 75005 Paris, France. [4]Université Paris Cité, 85 boulevard Saint-Germain, 75006 Paris, France. [5]New Zealand Institute for Advanced Study, Massey University, Auckland 0745, New Zealand. [6]Department of Molecular Biology, Umeå University, Umeå, Sweden. [7]Laboratory for Molecular Infection Medicine Sweden, Umeå Centre for Microbial Research, SciLifeLab, Umeå Centre for Microbial Research, Umeå University, Umeå, Sweden. [8]Department of Microbial Population Biology, Max Planck Institute for Evolutionary Biology, Plön 24306, Germany. [9]Laboratoire Biophysique et Évolution, CBI, ESPCI Paris, Université PSL, CNRS, 75005 Paris, France. [10]School of Biological Sciences, University of Canterbury, Christchurch 8041, New Zealand.

[†]School of Biological Sciences, Victoria University of Wellington, PO Box 600, 6140, Wellington, New Zealand.

[⌘]These authors contributed equally to this work.
[¥]Co-senior and co-corresponding authors: Rainey (rainey@evolbio.mpg.de), Desprat (desprat@ens.fr) and Hendrickson (heather.hendrickson@canterbury.ac.nz)

Abstract

Maintenance of rod-shape in bacterial cells depends on the actin-like protein MreB. Deletion of *mreB* from *Pseudomonas fluorescens* SBW25 results in viable spherical cells of variable volume and reduced fitness. Using a combination of time-resolved microscopy and biochemical assay of peptidoglycan synthesis, we show that reduced fitness is a consequence of perturbed cell size homeostasis that arises primarily from differential growth of daughter cells. A 1,000-generation selection experiment resulted in rapid restoration of fitness with derived cells retaining spherical shape. Mutations in the peptidoglycan synthesis protein Pbp1A were identified as the main route for evolutionary rescue with genetic reconstructions demonstrating causality. Compensatory *pbp1A* mutations that targeted transpeptidase activity enhanced homogeneity of cell wall synthesis on lateral surfaces and restored cell size homeostasis. Mechanistic explanations require enhanced understanding of why deletion of *mreB* causes heterogeneity in cell wall synthesis. We conclude by presenting two testable hypotheses, one of which posits that heterogeneity stems from non-functional cell wall synthesis machinery, while the second posits that the machinery is functional, albeit stalled. Overall, our data provide support for the second hypothesis and draw attention to the importance of balance between transpeptidase and glycosyltransferase functions of peptidoglycan building enzymes for cell shape determination.

Keywords: Cell shape – Experimental evolution – Single cell – Compensatory evolution – aPBPs – Cell wall – Rod complex

Introduction

The rescue of fitness-compromised mutants by selection is a useful strategy to obtain new understanding into the molecular determinants of complex phenotypes (Remigi et al. 2019; LaBar et al. 2020). The approach has shed light on factors such as the flexibility of regulatory networks (Lind et al. 2015), the diversity of structural components affecting ecological success (Lind et al. 2017), the predictability of evolution (Lind et al. 2019), the origins of new genes (Näsvall et al. 2012), and the causes of changes in interactions among bacteria and their hosts (Remigi et al. 2014). Here we turn attention to the evolutionary rescue of a *Pseudomonas fluorescens* mutant lacking MreB, a key component of cell shape (Errington 2003) that is conserved in a broad range of rod-shaped bacteria (Shi et al. 2018).

For model organisms, notably, *Escherichia coli* and *Bacillus subtilis*, the molecular mechanisms underpinning cell shape have been the subject of intensive investigation (Shi et al. 2018; van Teeffelen and Renner 2018; Egan et al. 2020). The primary determinant of bacterial cell shape in both Gram positive and Gram negative cells is peptidoglycan. Its synthesis and assembly is directed by two main multiprotein complexes that each comprise a combination of enzymes and regulatory elements involved in cell wall dynamics, DNA segregation and cell division (Daniel and Errington 2003; Young 2003; Osborn and Rothfield 2007; Young 2007; Huang et al. 2008; Young 2010). The first of these, the elongasome (or rod complex), inserts newly synthesised peptidoglycan strands into the lateral wall of the growing cell, while the divisome participates in septum positioning and cell wall constriction (van Teeffelen and Renner 2018). Both elongasome and divisome rely on penicillin-binding proteins (PBPs) to polymerize (transglycosylate) and / or to cross-link (transpeptidate) newly synthesised peptidoglycan strands.

The elongasome consists of several catalytically interacting components including the transglycosylase (TGase) RodA (Cho et al. 2016), the transpeptidase (TPase) Pbp2 (Ishino et al. 1986), that function in concert with class the A PBP (aPBP), Pbp1A, which has both TGase and TPase activities (Randich and Brun 2015). Activity of Pbp1A, while not strictly a member of the elongasome, depends on the outer membrane-anchored protein LpoA (Sardis et al. 2021), with Pbp1A interacting with Pbp2 (Banzhaf et al. 2012; Egan et al. 2020; Kang and Boll 2022). Central to elongasome function – and essential for construction of rod-shaped cells – is the actin-like protein MreB. MreB forms helical-like structures tethered to

the inner membrane and coordinates the pattern of new wall growth along the lateral part of the cell cylinder through interactions with other components of the elongasome (Typas et al. 2012; Shi et al. 2018). Indicative of a balance between diffusive synthesis affected by class A PBPs and processive activities of the elongasome is the fact that deletion of classA PBPs leads to up-regulation of rod complex activity (Patel et al. 2020), with evidence suggesting that the two systems work semi-autonomously (Cho et al. 2016).

Most bacteria contain a second aPBP, Pbp1B, which like Pbp1A, has both TGase and TPase activity. The two aPBPs are partially redundant (Yousif et al. 1985), but based on localisation of Pbp1B to the mid-cell during division (Bertsche et al. 2006), the standard view is that Pbp1B contributes to divisome function (particularly through interaction with PBP3), whereas Pbp1A contributes to cell elongation (Egan et al. 2020). However, it is apparent that Pbp1B also contributes to elongation (Typas et al. 2012; Cho et al. 2016), with evidence from *E. coli* that its role may be more important than Pbp1A (Vigouroux et al. 2020). In particular it was recently shown that Pbp1B responds to cell wall damage by repairing defects (Vigouroux et al. 2020) and that the bound (enzymatically active) form of Pbp1B is elevated in the absence of Pbp1A (Vigouroux et al. 2020).

In both *E. coli* and *B. subtilis* (and most other rod-shape bacteria), MreB is required for maintenance of rod-shape (Shi et al. 2018). While deletion of the gene is lethal under normal growth conditions, inhibition of MreB function by depolymerisation via the drug A22 causes abnormal cell wall growth leading to spherical cells that swell and eventually lyse (Iwai et al. 2002). An earlier study in *B. subtilis* – where cells devoid of MreB were maintained in a viable state by culture in the presence of magnesium – found that transposon-induced mutations in *pbp1A* could rescue cell viability in the absence of magnesium, but could not return cells to rod-shape (Kawai et al. 2009).

Here, with interest in evolution of the machinery underpinning cell shape, we took advantage of prior knowledge that inactivation of *mreB* in the rod-shaped bacterium *P. fluorescens* SBW25, while reducing fitness, is not lethal (Spiers et al. 2002), and asked whether selection could compensate for this cost. Of particular interest was: 1, the capacity for compensatory evolution to restore fitness; 2, the number, timing and impact of fitness-restoring mutations and; 3, the connection between fitness-restoring mutations, growth dynamics and cell morphology.

Materials and Methods

Bacterial strains and culture conditions

Escherichia coli and *Pseudomonas aeruginosa* were grown at 37°C; and *P. fluorescens* SBW25 at 28°C. Antibiotics were used at the following concentrations for *E. coli* and / or *P. fluorescens* SBW25: 12 µg ml^{-1} tetracycline; 30 µg ml^{-1} kanamycin; 100 µg ml^{-1} ampicillin. Bacteria were propagated in Lysogeny Broth (LB: 10 g tryptone, 5 g yeast extract, 10 g NaCl per litre).

Strain construction

The Δ*mreB* and Δ*pbp1A* mutants were constructed using SOE-PCR (splicing by overlapping extension using the polymerase chain reaction), followed by a two-step allelic exchange protocol[1]. All media for construction of *mreB* mutants were supplemented with 10 mM $MgCl_2$. Genome sequencing confirmed the absence of suppressor mutations. The same procedure was used to reconstruct the mutations from the evolved lines (*pbp1A* G1450A, *pbp1A* (A1084C), Δ*pflu4921-4925* (5399934-5403214del)) and ectopic Mini-Tn*7*T-*mreB* into ancestral SBW25 and Δ*mreB* backgrounds. DNA fragments flanking the mutation of interest were amplified using two primer pairs. The internal primers were designed to have overlapping complementary sequences that allowed the resulting fragments to be joined together in a subsequent PCR reaction. The resulting DNA product was TA-cloned into pCR8/GW/TOPO (Invitrogen). This was then subcloned into the pUIC3 vector, which was mobilised via conjugation into SBW25 with the help of pRK2013. Transconjugants were selected on LB plates supplemented with nitrofurantoin, tetracycline and X-gal. Allelic exchange mutants identified as white colonies were obtained, where possible, by cycloserine enrichment to select against tetracycline resistant cells, and tetracycline sensitive clones were examined for the deletion or mutations using PCR and DNA sequencing. Complementation of *mreB* in the Δ*mreB* background was achieved by cloning the PCR-amplified DNA fragment into pUC18-mini-Tn*7*T-LAC, which was subsequently integrated into the *P. fluorescens* SBW25 genome at a unique site located downstream of the *glmS* gene (Liu et al. 2014).

Growth dynamics

Strains were initially grown in 5 mL LB broth at 28ºC overnight, except for Δ*mreB* which was grown for 2 days. Growth curves were started by adding 2 µl aliquots of overnight

cultures to LB to a final volume of 200 µl (1:100 dilution) in 96-well microplates (3 replicates). Plates were incubated at 28ºC (with shaking) for 24 to 48 hours in a BioTek Synergy 2 plate reader. Growth was measured at an absorbance of 600 nm and recorded at 5-minute intervals using the Gen5 software (Bio-Tek). Growth curves were processed as semi-log plots to identify the lag and exponential phases. Doubling times were calculated as: t = ln (2)/k.

Evolution experiment

Ten replicate populations of the Δ*mreB* strain were grown in 5 mL aliquots of LB broth at 28°C with shaking at 180 rpm. Every 24 h, 5 µL was transferred to fresh media. Every 5 days, samples of each population were collected and stored at -80°C in 15% (v/v) glycerol. The number of generations per transfer changed over the course of the experiment but was approximately ten generations per 24 h period (100 transfers (~1,000 generations) were performed).

Competitive fitness assay

Competitive fitness was determined relative to ancestral SBW25 marked with GFP. This strain was constructed using the mini-Tn7 transposon system, expressing GFP and a gentamicin resistance marker (mini-Tn7 (Gm)P_{rrnB} P1 gfp-a). Strains were grown to exponential phase in shaken LB at 28°C before beginning competitive fitness assays. Competing strains were mixed with SBW25-GFP at a 1:1 ratio by adding 150 uL of each strain to 5 mL LB and grown for 3 hours. Initial ratios were determined by counting 100,000 cells using flow cytometry (BD FACS Diva II). Suitable dilutions of the initial population were plated on LB agar plates to determine viable counts. The mixed culture was diluted 1,000-fold in LB, then incubated at 28°C for 24 hours. Final viable counts and ratios were determined as described above. The number of generations over 24 hours of growth were determined using the formula ln(final population/initial population)/ln (2). Selection coefficients were calculated using the regression model $s = [\ln (R(t)/R(0))]/[t]$, where R is the ratio of the competing strain to SBW25-GFP, and t is time. Control experiments were conducted to determine the fitness cost of the GFP marker in SBW25. For each strain, the competition assay was performed with a minimum of three biological replicates. Ancestral SBW25 had a relative fitness of 1.0 when compared to the marked strain, indicating that the GFP insert is neutral, and that the SBW25-GFP strain was a suitable reference strain for this assay.

Mutation detection

In order to detect mutations in the experimental lines, total DNA was extracted from the Δ*mreB* strain and from each of the 10 populations at 500 and 1,000 generations. Samples were submitted for 100 bp single-end Illumina DNA sequencing at the Australian Genome Research Facility in 2012. An average of 6,802,957 single reads were obtained per sample and these were assembled against the reference *P. fluorescens* SBW25 genome (GenBank accession: OV986001.1) using the clonal option of Breseq with default parameters (Deatherage and Barrick 2014). Mutations were identified with breseq's HTML output and in the case of predicted novel junctions manually inspected with Geneious Prime (https://www.geneious.com). The raw sequence files and breseq-generated data outputs are available at https://doi.org/10.17617/3.CU5SX1.

To detect the frequency of the *pbp1A* mutations in experimental lines at generation 50 a colony sequencing approach was used. Colony sequencing was used to prevent the confounding effects of altered cell size, and genomic content per cell, on estimates of the frequency of mutants. To ensure sequenced colonies were isogenic, the frozen glycerol stock from generation 50 was streaked on LB agar plates and individual colonies were each re-streaked on LB agar. Resulting colonies were then used as a template for PCR, using primers that allowed amplification of all the mutations identified by Illumina Sequencing at 500 and 1000 generations. Sanger sequencing was used to identify mutations, with mutations only called if present in sanger sequencing from both forward and reverse primers, with sequences mapped to the *pbp1A* sequence from the SBW25 reference genome using Geneious Prime.

Microscopy

Phase contrast and fluorescence images were captured using the BX61 upright microscope (Olympus) at 100x using a Hamamatsu Orca Flash 4.0 camera. The microscope is equipped with an HXP lamp with appropriate multi-band pass filters for different channels. Cell^P/ Cellsens software (Olympus) was used to control the microscope. Cells were grown in LB, and harvested at log phase (OD_{600} 0.4). Viability assays were conducted using the LIVE/DEAD BacLight Bacterial Viability Kit (Thermo Fisher). Viability was measured as the proportion of live cells in the total population (live/ (live +dead)). Nucleoid staining was performed using the DAPI nucleic acid stain (Thermo Fisher) following the manufacturer's protocols.

Time-lapse on agarose pads

Strains were inoculated in LB from glycerol stocks and grown with shaken overnight at 28°C. Cultures were then diluted 100-fold in fresh LB and seeded on a gel pad (1% agarose in LB). The preparation was sealed on a glass coverslip with double-sided tape (Gene Frame, Fischer Scientific). A duct was cut through the center of the pad to allow for oxygen diffusion into the gel. Temperature was maintained at 30°C using a custom-made temperature controller. Bacteria were imaged on a custom-built microscope using a 100X/NA 1.4 objective lens (Apo-ph3, Olympus) and an Orca-Flash4.0 CMOS camera (Hamamatsu). Image acquisition and microscope control were actuated with a LabView interface (National Instruments) (Julou et al. 2013). Typically, we monitored 10 different locations; images were taken every 5 min in correlation mode. Segmentation and cell lineage were computed using a MatLab code implemented from Schnitzcell (Locke and Elowitz 2009). Bacteria were tracked for 3 generations. In order to limit the number of generations, we monitored bacteria harvested from a liquid stationary phase. Since, bacteria shorten after entering stationary phase, bacteria lengthened when resuming growth under the microscope, so that the elongation rate is larger than the septation rate for the first generations (Fig. 3B). To obtain the control line in our experimental configuration, we measured these rates in three species (ancestral *P. fluorescens* SBW25, *E. coli* MG1655 and *P. aeruginosa* PAO1). Points below the line indicate a reduction of cell volume beyond the fact that cells simply resumed growth.

Scanning Electron Microscopy (SEM).

Cells were grown in LB, and harvested in log phase. Cells were fixed in modified Karnovsky's fixative then placed between two membrane filters (0.4µm, Isopore, Merck Millipore LTD) in an aluminum clamp. Following three washes of phosphate buffer, the cells were dehydrated in a graded-ethanol series, placed in liquid CO_2, then dried in a critical-point drying chamber. The samples were mounted onto aluminum stubs and sputter coated with gold (BAL-TEC SCD 005 sputter coater) and viewed in a FEI Quanta 200 scanning electron microscope at an accelerating voltage of 20kV.

Image analysis

Compactness and estimated volume measurements of cells from liquid culture. The main measure of cell shape, compactness or C, was computed by the CMEIAS (Liu et al. 2001)

software as: √ (4Area/π)/major axis length (Liu, J. 2001). Estimated volume or V_e was estimated with different formula, according to cell compactness, for spherical cells that have a compactness ≥ 0.7, V_e was computed using the general formula for ellipsoids: V=4/3π (L/2) $(W/2)^2$, where L=length and W=width. V_e of rod-shaped cells, defined as having a compactness value ≤ 0.7, were computed using the combined formulas for cylinders and spheres: $V_e = (\pi (W/2)^2 (L-W)) + (4/3\pi (W/2)^3)$.

Cell volume and division axis of cells on agarose pads. Cell volume was computed from the mask retrieved after image segmentation. Masks were fitted to an ellipse. The elongation axis is given by the direction of the major axis. The division axis relative to the mother was computed by comparing the elongation axis between mother and sister cells using the following formula: $|sin\theta|$, where θ is the angle between mother and sister cells. $|sin\theta|$=0 means that mother and daughter cells are aligned, $|sin\theta|$=1 means that they are perpendicular.

Probability p to pass to the next generation: For the second generation on the agar pad, we computed the probability to pass to the next generation as the capability of cells to progress through the cell cycle and divide. Bacteria that did not grow or stopped elongating before dividing were classified as non-proliferating. For all non-proliferating bacteria, we confirmed that no division occurred during the next 5 hours. The p ratio was then simply computed as the number of viable daughter cells divided by the expected number. Error on the probability is estimated at the 95% confidence interval by the formula: $1.96\sqrt{p(1-p)/N}$, where N is the total number of cells.

Elongation rate, septation rate, growth asymmetry and the precision of septum positioning: The elongation rate, r, measured in min^{-1} is the rate at which cell volume increases: $V(t)=V_0e^{rt}$, where t is the relative time in the cell cycle. The septation rate is given by $\frac{ln\ (2)}{\tau}$, where τ is the average division time, *i.e.*, the time between birth and septation. For all sister cell pairs, we computed relative difference in growth between sister cells by measuring the relative elongation rate (*i.e.*, volume extension rate) of sister cells at generation F1: $|\frac{r_2-r_1}{r_1+r_2}|$, where $r_{1,2}$ is the elongation rate for each cell of sister pairs. The population average C_g=<abs $(r_1-r_2)/(r_1+r_2)>_{cells}$. was computed on the proliferating sub-population in order to avoid trivial

bias due to cell proliferation arrest of one of the two sister cells. We did the same for the relative difference in division time and measured C_T=<abs (T_1-T_2)/ (T_1+T_2)>$_{cells}$., where $T_{1,2}$ are the division time of sister cells. For all cells at generation F1, we computed the precision of septum positioning by measuring the relative cell volume of the two daughter cells: $|\frac{V-V_1}{V+V_2}|$, where $V_{1,2}$ are the volumes of each daughter cell. The population average C_s=<abs (V_1-V_2)/ (V_1+V_2)>$_{cells}$ was computed for every F1 cell having offspring.

Laplace argument

For a given geometry, cell volume is determined, at steady state, by an analog of the Young-Laplace law for thin elastic membranes, which relates the pressure discontinuity ΔP at the cell wall to membrane tension and radius of curvature R_s. The pressure jump is powered by turgor pressure in the cytoplasm. For spheres, having two identical curvature radii R_s, the law is $\Delta P_S = \frac{2T_S}{R_s}$. For cylinders, having only one finite radius of curvature R_c, the law is $\Delta P_C = \frac{T_C}{R_C}$. Assuming that turgor pressure and membrane tension are the same, $\Delta P_S = \Delta P_C$ and $T_S = T_C$, we obtain $R_s = 2R_c$. Hence, the ratio of volumes between the two geometries can be expressed as a function of the original ancestral SBW25 length L and width $2R_c$: $\frac{V_s}{V_c} = \frac{2^5 R_c}{3L}$, where V_s and V_c are the volume of the sphere and the cylinder, respectively. Hence a change from cylindrical to spherical shape should result in a volume increase by a factor 1.78 for *P. fluorescens*, with a diameter of 1µm and a length of 3µm (Fig. 3A).

Protein sequence alignment and modelling

Protein sequences were obtained from NCBI BLAST (http://blast.ncbi.nlm.nih.gov) and The *Pseudomonas* Genome Database (Winsor et al. 2016), and aligned using MEGA7 (Kumar et al. 2016). The sequence alignment was visualised using ESPript 'Easy Sequencing in PostScript' (Robert and Gouet 2014). Protein visualisation was performed using Visual Molecular Dynamics (VMD) (Humphrey et al. 1996) based on the crystal structure of *Acinetobacter baumannii* Pbp1a in complex with Aztreonam as the base model (Pbp1A from *A. baumannii* shares a 73% amino acid sequence identity (E value = 0.0) to the Pbp1A of *P. fluorescens* SBW25). Sequences were aligned, and locations of the mutations in the evolved lines were mapped in the corresponding regions. The PDB file was downloaded from the RCSB Protein Data Bank (www.rcsb.org) using PDB ID 3UE0.

Membrane preparation and detection of penicillin-binding proteins

For the membrane preparation of the different genotypes of *P. fluorescens* SBW25, 150 mL cell cultures were grown to an OD_{600} of 0.6 and harvested by centrifugation at 15,000 x g for 15 minutes at 4 °C (Beckman JLA-16.250 rotor, Beckman Avanti J-25, Beckman Coulter). Pellets were washed with 20 mM potassium phosphate (pH 7.5) and 140 mM sodium chloride buffer. Following another 30 minutes of centrifugation at 360 x g at 4 °C, cells were disrupted by passing twice through a French press ('Pressure Cell' Homogenizer FPG12800, Stansted Fluid Power Ltd). Cell lysates were subjected to centrifugation at 360 x g for 10 minutes at 4 °C. Supernatant fractions were collected and centrifuged at 75,600 x g for 90 minutes at 4 °C (Beckman JA25.50 rotor, Beckman Avanti J-25, Beckman Coulter). The resulting pellets were washed once again and resuspended in 100 µL potassium phosphate buffer. The concentration of the membrane preparations was measured using Bradford reagent (BioRad) with bovine serum albumin as a standard (Sigma).

For detection of PBPs, membranes were incubated for 30 minutes at 37 °C with a fluorescent labelling agent, Bocillin FL Penicillin (Invitrogen, Thermo Fisher Scientific) (final concentration: 0.05 mM). Finally, the samples were denatured with 5x SDS loading buffer with ß-mercaptoethanol as a reducing agent at 100 °C for 5 minutes, followed by centrifugation to remove membrane debris. 20 µL of reaction mixture was subjected to SDS-PAGE analysis on an 8% polyacrylamide gel, protected from the light. Bocillin FL-labelled PBPs were visualised with a laser scanner, Typhoon FLA 9500 (GE Healthcare Life Sciences) at 473 nm with a 530DF20 emission filter.

Peptidoglycan isolation and analysis

For peptidoglycan profiling and analysis, *P. fluorescens* genotypes were grown in LB medium to an OD_{600} of 0.2 and harvested. Purification of peptidoglycan was carried out as previously described (Desmarais et al. 2013) with some minor changes. Briefly, the cell pellets were boiled in an equal volume of 5% (w/v) SDS for approximately an hour and left stirring overnight at room temperature. The sacculi were washed repeatedly with MilliQ water by ultracentrifugation (150 000 × g, 15 min, 20 °C TLA100.3 Beckman rotor; OptimaTM Max ultracentrifuge Beckman, Beckman Coulter) until SDS was eliminated from the samples. The clean sacculi were digested with muramidase (Cellosyl 100 $\mu g.mL^{-1}$) overnight at 37 °C. The enzyme reaction was stopped by heat-inactivation at 100 °C. Coagulated proteins were removed by centrifugation (21,000 x g for 15 min, Heraeus™

Pico™ 21 Microcentrifuge, Thermo Fisher Scientific). For sample reduction, supernatants were adjusted to pH 8.5 - 9.0 with borate buffer, followed by incubation for 30 minutes at room temperature with freshly prepared $NaBH_4$ solution (final concentration of 10 $mg.mL^{-1}$). Finally, the pH was adjusted to 3.5 by the addition of phosphoric acid. Muropeptides were separated by UPLC on a Waters UPLC system (Waters) equipped with a Kinetex C18 UPLC Column, 130 Å, 1.7 µm, 2.1 mm × 150 mm (Phenomenex) and a dual wavelength absorbance detector. Elution of muropeptides was detected at 204 nm. Separation of the muropeptides was carried out at 45 °C using a linear gradient from Buffer A (formic acid 0.1% (v/v) to Buffer B (formic acid 0.1% (v/v), acetonitrile 40% (v/v) in an 18 min run with 0.250 $mL.min^{-1}$ flow.

Fluorescent D amino acid labeling:

Short-pulse staining of FDAA incorporation into growing *P. fluorescens* cell walls was accomplished using FDAA BODIPY-FL 3-amino-D-alanine (BADA) (Hsu et al. 2017) (green; emission 502 nm, excitation 518 nm). Briefly, BADA was diluted in dimethyl sulfoxide to a concentration of 100 mM. For each test strain, one mL of exponential culture (OD 600 of 0.4) was pelleted by centrifugation (10,000g : 2,000g for *ΔmreB*) and resuspended in 100 uL. BADA was added to achieve a final concentration of 1mM BADA. Incubation at 28°C for 20% of strain generation time. Following this, 230 µL of ice-cold 100% ethanol was added to culture. An additional 1 mL of ice cold 70% ethanol was added to remove excess dye. Cells were fixed on ice for 15 minutes before being washed with 1 mL of PBS three times to remove excess BADA. Finally, cells were resuspended in 20-100 µL of PBS and subjected to standard fluorescent microscopy on agarose pads. Fluorescent microscopy was performed as described above.

Results

Deletion of *mreB* from *P. fluorescens* SBW25 generates viable spherical cells

Previous observations of viable *mreB* mutants of SBW25 came from transposon screens of adaptive (wrinkly spreader) mutants (Spiers et al. 2002). To establish that cells can indeed proliferate despite the absence of MreB, *mreB* was deleted from ancestral *P. fluorescens* SBW25 (hereafter SBW25). In LB broth, SBW25 Δ*mreB* cells were viable, spherical and variable in cell volume (Fig. 1A). DNA sequencing showed no evidence of cryptic compensatory mutations (see breseq output https://doi.org/10.17617/3.CU5SX1).

Cell shape, width and length were used to estimate volume (V_e). The volume of Δ*mreB* mutant cells was larger (20.65 ± 16.17 μm^3) than those of ancestral SBW25 (3.27 ± 0.94 μm^3) cells. A negative correlation between V_e and compactness (the ratio of spherical to circle shape with a compactness of 1.0 being a circle) as a result of cell elongation was evident for SBW25 (R^2 = 0.63) (Fig. 1B). In contrast, only a weak correlation was observed for the Δ*mreB* mutant (R^2 = 0.13) (Fig. 1B). As cell volume increases, DNA content is expected to increase provided that DNA replication continues independently of septation. Increased DNA content and spherical cell shape are both predicted to further perturb cell division (Jun and Mulder 2006; Jun and Wright 2010). Ancestral SBW25 and Δ*mreB* cells were stained with a nucleic acid stain (DAPI) and analysed using flow cytometry. In both genotypes DNA content scaled with cell volume. The largest Δ*mreB* cells had many times the DNA content of ancestral cells, scaling approximately with volume (Supp. Fig. 1, Supp. Fig. 2); small cells yield a signature consistent with maintenance of DNA (Supp. Fig. 1).

In comparison with SBW25, the Δ*mreB* mutant had reduced fitness (Fig. 1C) with a longer effective generation time, extended lag phase, and lower maximum yield (Supp. Fig. 3). Complementation of Δ*mreB* with the ancestral gene restored rod-shaped morphology and fitness (Supp. Fig. 4).

To understand the causes of reduced fitness, the division of single cells was monitored by time-lapse video microscopy on agar pads. Although SBW25 Δ*mreB* cells appear spherical, measurement of cell aspect ratio revealed existence of an elongation axis that remained constant throughout the cell cycle (Supp. Fig. 5). As in rod- and ovococci-shaped bacteria, the septum formed perpendicularly to the elongation axis. After cell division, the elongation

axis rotated 90º relative to the mother cell (Supp. Fig. 6, Supp. Movie 1), which is reminiscent of ovococci (Pinho et al. 2013). But more surprisingly, measurement of the rate of volume extension (hereafter termed elongation rate measured in min^{-1}) showed that during exponential phase it was indistinguishable from the cell elongation rate of ancestral SBW25 (Fig. 1D).

Since elongation rate was unchanged upon deletion of *mreB*, reduced fitness of the mutant was likely due to production of non-viable cells. We thus measured cell viability in LB broth with a "live / dead" assay and showed that 95% of ancestral SBW25 cells were viable, while the fraction of viable Δ*mreB* mutant cells was reduced to 81%. Thus, the decreased fitness of the mutant is primarily a consequence of the production of non-viable cells (Fig. 1E). To confirm this result, we performed time lapse microscopy of cells grown on agar pads to measure the probability p to pass to the next generation. For ancestral SBW25, the probability p of producing offspring equals 1, whereas for Δ*mreB* cells, $p = 0.85$. In instances where the probability to pass to the next generation p is not equal to one, the equation for growth dynamics is represented by $dN=p*r*N*dt$, where N is the number of cells at time t and r is the cell elongation rate. Hence, the effective growth rate of the population is given by $p*r$. Because Δ*mreB* and ancestral SBW25 cells elongate at the same rate, the fitness of Δ*mreB* cells is directly given by p. Consistently, the probability to pass to the next generation $p = 0.85\pm0.05$ (N=141), as measured in single cell experiments, is not significantly different from the fitness of 0.77±0.025 for Δ*mreB* in bulk experiments (Fig. 1C).

We next examined the causes for decreased proliferation capacity by measuring, at the single cell level, the correlation between the probability p to pass to the next generation and the fidelity of cell division. To this end, the precision of septum positioning, C_s, and correlation between the relative difference in elongation rate between sister cells at generation F1, C_g, and probability p of producing offspring at the end of generation F1 (Fig. 1F) were calculated. As a proxy to determine the precision of septum positioning, we measured the relative difference C_s in cell volume V_e, between two daughter cells immediately after division at generation F2. In ancestral SBW25, septum position was accurately placed, with only 5 % difference in the volume of sister cells. In Δ*mreB* mutant cells, the accuracy of septum position was significantly altered, with 19.4 % difference in the volume of sister cells. To determine if sister cells had different growth dynamics, we measured the relative difference C_g in elongation rate r between two sister cells at generation F1. In ancestral

SBW25, the elongation rate in pairs of sister cells differed by 5 %, whereas in Δ*mreB* cells the difference in rate was on average 55 %. Combined together, error in septum positioning and growth asymmetry between sister cells explains why the Δ*mreB* mutant produces cells of variable volume, which then have different proliferative capacity. To examine how cell volume affects proliferation ability, the probability *p* to pass to the next generation was plotted as a function of cell volume. As evident in Fig. 1G the volume distribution has two extreme tails, with both large and small cells being unlikely to produce viable offspring.

Selection rescues fitness of a compromised *mreB* deletion mutant

To determine whether selection could discover mutation(s) that might compensate for reduced fitness of Δ*mreB*, SBW25 Δ*mreB* was propagated for 1,000 generations in shaken broth culture with daily transfer. The competitive fitness of derived types was measured relative to ancestral SBW25 using neutral markers to distinguish competitors. Fitness of all replicate lines (relative to ancestral SBW25) significantly improved (Fig. 2A) to the point where fitness was comparable to ancestral SBW25 (Supp. Fig. 7). Subsequent measurement of fitness at generations 50, 250 and 500 showed that compensation of fitness was rapid, with a highly similar trajectory for each of the 10 replicate populations (Supp. Fig. 8). Such rapid restoration of fitness is indicative of a small number of readily achievable compensatory mutations.

Examination of derived genotypes at generation 1,000 by microscopy showed that all lines retained the coccoid shape (Fig. 2B, Supp. Fig. 9). Cell volume decreased compared to that of the ancestral cell type (Fig. 2B) and did not overlap with the Δ*mreB* population (Fig. 1B and 2B) showing that the derived cells define a new phenotype and not a subset of the spherical Δ*mreB* ancestor. Analysis of the pattern of cell division in the derived lines showed evidence of an elongation axis, which rotated at cell division, as observed for Δ*mreB* mutant cells (Supp. Fig. 6).

Identifying compensatory mutations

In order to identify the genetic basis of adaptation, populations were sequenced at generations 500 and 1,000 with the ensuing reads mapped to the genome of SBW25 (Table 1) and mutations identified using Breseq (Deatherage and Barrick 2014). A single gene, *pbp1A* (PFLU0406) had mutations in seven independent lines. In four of these, Line 1 (D484N), Line 3 (D721A), Line 4 (T362P) and Line 6 (N698K), the mutation had risen to

high frequency, but only in Line 6 was the mutation fixed. Some lines (4, 9 and 10) had more than a single *pbp1A* mutation and in some instances the mutation detected at generation 500 differed from that evident at generation 1,000. Clonal interface between competing mutations thus seems likely. In the three lines, with no evidence of *pbp1A* mutations at generations 500, or 1,000, two exhibited mutations in genes involved in septum formation (*ftsA* for Line 2 and *ftsZ* for Line 5). Finally, Line 7, contained a five-gene deletion spanning PFLU4921 to PLFU4925 which included *oprD*, but also has a non-synonymous mutation in *ftsE* that was not detected at generation 500, but composed 65% of sequencing reads at generation 1,000. The prominence of *pbp1A* mutations led us to further study two lines showing *pbp1A* mutations (Line 1 and Line 4) and to compare them with the five gene deletion (PFLU4921 to PLFU4925 Δ5399934-5403214) evident in Line 7.

The *pbp1A* gene is a class A penicillin-binding protein with both transpeptidase (TP) and transglycosylase (TG) activities. It is semi-autonomous and interacts with the rod complex and specifically with PBP2 (Banzhaf et al. 2012; Geisinger et al. 2020). Pbp1A contains three known domains (Fig. 2C). Structure mapping of the mutations shows that the mutation in Line 1 occurred in the transpeptidase (TP) domain, which is proximal to the active site (Supp. Fig. 10). Similar mutations in *Streptococcus pneumoniae* cause a loss-of-function (Job et al. 2008) and rescue viability of both *mreC* and *mreD* mutants (Land and Winkler 2011). The mutation in Line 4 occurred in the oligonucleotide/oligosaccharide binding or outer membrane Pbp1A Docking Domain (OB/ODD) domain (Typas et al. 2012). Each mutation was reconstructed by allelic exchange in SBW25 and SBW25 Δ*mreB* backgrounds.

Given the very rapid fitness increase (Supp. Fig. 8) we looked for evidence of *pbp1A* mutations at generation 50. The gene was amplified by PCR from 16 colonies from each replicate population and the product Sanger sequenced. All lines had at least one mutation (out of the 16 colonies) demonstrating the relative ease at which *pbp1A* mutations arise. Results are shown in Supp. Table 2.

Analysis of *pbp1A* mutations

Both Δ*mreB pbp1A* reconstructed genotypes (hereafter Δ*mreB pbp1A**) produced spherical-to-ovoid cells with near ancestral SBW25 volume (Δ*mreB pbp1A* (D484N) M = 3.86±0.89 μm^3; Δ*mreB pbp1A* (T362P) M = 5.51±0.87 μm^3) and DNA content (Fig. 2B, Supp. Fig. 2). Analysis of the pattern of cell division in the reconstructed lines showed evidence of an

elongation axis that rotated at cell division as observed for SBW25 Δ*mreB* (Supp. Fig. 6). Δ*mreB pbp1A** genotypes showed growth dynamics and fitness effects similar to ancestral SBW25 (Supp. Fig. 11) (Fig. 2A), indicating that these *pbp1A* mutations are each sufficient to restore ancestral fitness and to recapitulate the major phenotypes of derived Lines 1 and 4. Elongation rate was identical to SBW25 for SBW25 Δ*mreB* carrying the reconstructed mutations, (Supp. Fig. 12). Fitness of a genetically engineered Δ*mreB* Δ*pbp1A* mutant (relative to Δ*mreB*) was 1.35 (SD±0.04, n = 6) was indistinguishable from fitness of the Line 4 mutation reconstructed in the same Δ*mreB* background (1.38; SD±0.11, n = 6) demonstrating that loss-of-function of *pbpB1A* is sufficient to restore fitness (Supp. Fig. 13). Loss-of-function is also consistent with the finding that at generation 50 all lines harboured mutations in *pbp1A* (Supp. Table 2).

When reconstructed in ancestral SBW25, *pbp1A* mutations had little effect on population dynamics (Supp. Fig. 11A), or shape (Fig. 2B), however, elongation rates were reduced (Supp. Fig. 12), suggesting that the *pbp1A* mutations result in a reduction – or more likely even complete loss-of-function. In addition, cells were narrower than WT cells: 0.89 µm (SD±0.07) and 0.94 µm (SD±0.05) for Pbp1A TP and OB/ODD mutations, respectively, compared to 1.00 µm (SD±0.06) for ancestral SBW25. This resulted in smaller cell volumes (Fig. 2B, Supp. Figs 14 & 15). The reduced widths / volumes -- which also correlate with reduced DNA content (Supp. Fig. 2) – might be indicative of reduced enzymatic function leading to reduced lateral cell wall synthesis as the case for loss-of-function mutations in *pbp1A* reported in both *B. subtilis* and *E. coli* (Murray et al. 1998; Claessen et al. 2008; Kawai et al. 2009; Banzhaf et al. 2012).

Analysis of Δ*pflu4921-4925*

The five-gene deletion (Δ5399934-5403214 (Δ*pflu4921-4925*)) in derived Line 7 (Supp. Fig. 16, Supp. Table 1) includes three hypothetical proteins, a cold shock protein (PFLU4922, encoding CspC), and an outer membrane porin, PFLU4925, which encodes OprD. The latter is responsible for the influx of basic amino acids and some antibiotics into the bacterial cell (Skurnik et al. 2013). The deletion was also reconstructed and characterised in the Δ*mreB* and ancestral SBW25 backgrounds. The relative fitness of the Δ*mreB* Δ*pflu4921-4925* genotype was similar to the ancestral SBW25 type (Fig. 2A), but with an extended lag time (Supp. Fig. 11). Cells were spherical with an average Ve of 5.26 μm^3 (SD±3.13) (Fig. 2B, Supp. Figs 14 & 15) and harboured less DNA compared to Δ*mreB* SBW25, but more than

the Pbp1A* reconstructions in the same background (Supp. Fig. 2). In addition, a fraction of the cell division events were defective, resulting in clumps of spherical cells with imperfectly formed septa (Fig. 2B, Supp. Fig. 14-17). Spherical cells with notably incomplete septa were not observed in the derived Line 7 population (Supp. Table 1).

When genes *pflu4921-4925* (Δ5399934-5403214) were deleted from ancestral SBW25 the cells remained rod-shaped and displayed aberrant growth characteristics relative to the ancestral strain (Supp. Fig. 14). The elongation rate was slower (Supp. Fig. 12), cells were significantly thinner (width = 0.74µm SD±0.06; $p < 0.001$, two sample *t*-test), and had a smaller average Ve (2.47 μm^3, SD±1.18) (Fig. 2B and Supp. Fig. 15). As in the Δ*mreB* background, a fraction of cells failed to completely separate at cell division and DNA was dispersed between incomplete septa (Supp. Figs 14-17). The average DNA content of SBW25 Δ*pflu4921-4925* cells was greater than the *pbp1A** reconstructions in the same background (Supp. Fig. 2).

Cell volume homeostasis

The large average cell volume observed in stationary phase SBW25 Δ*mreB* cells (Fig. 2B) suggests that some of the physical parameters governing cell volume may have been altered. Cell volume at steady state is determined by the equilibrium between turgor pressure (Rojas and Huang 2018) and membrane tension through the Laplace law for thin elastic shells (Verge-Serandour and Turlier 2021) (see Materials and Methods for elaboration). Since it is difficult to imagine a scenario where the cell-wall would strengthen in the absence of *mreB*, *mreB* loss is expected to result in a significant decrease of internal pressure compared to ancestral SBW25 cells, synonymous with the influx of water through pores formed in the cell-wall.

During exponential growth, the cell volume of daughter cells is limited by the amount of new material that can be incorporated by the mother cell. According to the "adder" model (Campos et al. 2014; Taheri-Araghi et al. 2017), the average cell volume in the population converges within a few generations towards the average added volume. We thus quantified the added volume for all strains (Fig. 3A) and confirmed that cell volume rapidly reduced for exponentially growing SBW25 Δ*mreB* cells (Supp. Movie 2). Since, the volume of Δ*mreB* cells in exponential phase is much lower than in stationary phase, it suggests that cells swell during stationary phase, probably due to defects in cell wall integrity with deleterious

consequences for cell viability. Hence, without restoring cell wall integrity, cell volume homeostasis cannot be maintained. Remarkably, the added-volumes of spherical cells in each of the derived mutant lines (Fig. 3A) were close to the volumes corresponding to the passage from a cylindrical to spherical geometry with constant turgor pressure and membrane tension (see Materials and Methods). This suggests that adaptive mutations restored the mechanical integrity of the cell wall.

To maintain cell volume homeostasis, elongation and septation rates must be balanced so that cells maintain a steady volume throughout successive generations. Indeed, if septation is faster than elongation, cell volume of progeny decreases, while if elongation is faster than the rate of septation rate, cells increase in volume. In both instances the fate of populations is extinction. The rate of septation was significantly higher than the elongation rate in Δ*mreB* cells showing that the distribution of cell volume is unstable and confirms that the average volume is expected to decrease in subsequent generations (Fig. 3B). In contrast to SBW25 Δ*mreB* cells, the rates of elongation and septation were balanced in the derived lines (Fig. 3B), indicating that cell volume homeostasis has been reached. Reconstruction of *pbp1A* mutations in SBW25 Δ*mreB* also restored this balance, suggesting that the mutations contribute to maintenance of volume homeostasis in the absence of *mreB*. In contrast, the Line 7 deletion reconstructed in SBW25 Δ*mreB* did not restore this balance (Fig. 3B,).

Another important feature for cell volume homeostasis is the fidelity of cell division: two daughter cells with equal volume must themselves generate four daughters of equal volume. Therefore, we measured the relative difference in elongation rates (C_g) and division time (C_T) between sister cells at generation F1 on agar pads, as well as the relative difference in precision of septum positioning (C_s) for all derived and reconstructed lines. All evolved lines regained symmetry both in elongation rate and in precision of septum positioning, but was most notable for the symmetry of elongation rate (Fig. 3C & D). These improvements correlate with an increase in proliferative capacity, while no significant correlation was observed in the relative difference of division time C_T between sister cells (Supp. Fig. 18). Reconstructions in ancestral SBW25, showed a slight alteration of symmetry, which is more pronounced in the case of Line 7 (five gene deletion). Reconstructions in evolved lines Line 1 and Line 4 showed improvement in growth asymmetry. Interestingly, recovery was only partial for Line 7, raising the possibility of additional effects due to a secondary mutation whose effects depend on the mechanics of the environment (liquid vs solid culture). Indeed,

as indicated above and shown in Supp. Table 1, Line 7, at generation 1,000, also contains a non-synonymous mutation in *ftsE* (T188A) that had reached high frequency. Given that FtsE promotes elevated peptidoglycan synthesis at cell septa the possibility of synergistically beneficial effects with the OprD-inclusive deletion is not improbable (Mallik et al. 2023).

The mutations observed in Line 1 or Line 4 showed a significant improvement in the precision of septum position, suggesting that asymmetry in elongation rate between daughter cells has greater impacts on cell survival than septum positioning. This can also be seen from the shape of the curves (Fig. 3C & D), where *p* decreases linearly with growth asymmetry up to 50%, while precision of septum positioning saturates at 20% regardless of *p*, probably because nucleoid occlusion is able to achieve a sufficiently good level of septum positioning.

Investigating the molecular consequences of mutations

To obtain insight into the molecular mechanisms by which mutations in *pbp1A* compensate for loss of *mreB*, we performed a range of biochemical analyses on SBW25 and SBW25 Δ*mreB* engineered with the fitness-rescuing mutations in *pbp1A*: SBW25 / SBW25 Δ*mreB* Pbp1A (D484N) (mutation in the TPase domain); SBW25 / SBW25 Δ*mreB* Pbp1A (T362P) (mutation in the OB/ODD domain). SBW25 Δ*mreB* Δ*pbp1A* was used as a negative control. In ancestral SBW25 36.34% (SD±2.26) of muropeptides are cross-linked (Fig. 4A). The Δ*mreB* mutant showed a marked increase in cross-linking (40.47% SD±1.50). The degree of cross-linking in the *pbp1A* mutants in either SBW25 or the Δ*mreB* genetic background were lower (31.28% SD±0.98 to 33.66% SD±0.52).

Lower levels of cross-linking observed in the Δ*mreB* and SBW25 reconstructed lines suggests that mutations in Line 1 and 4 either decreased the amount of transpeptidation or increased the amount of transglycosylation. To discriminate between the two hypotheses, we utilised Bocillin-FL labelling, a fluorescent penicillin derivative that binds to the active site of PBPs, as a proxy to measure PBP1a TPase activity. We included SBW25 Δ*pbp1A* as a control to specifically identify the band corresponding to Pbp1A in the SDS-PAGE gel (Fig. 4B). In agreement with higher levels of cross-linking activity measured in SBW25 Δ*mreB* (Fig. 4A), the intensity of the Pbp1A band was slightly higher in Δ*mreB* cells compared to the ancestral genotype. In comparison to the ancestor of the evolved lines (SBW25 Δ*mreB*), this signal was little changed in the Line 1 mutant (TP domain (SBW25 Pbp1A (D484N)) (Fig. 4B), but absent in the Line 4 mutant (OB/ODD domain (SBW25 Pbp1A (T362P))). The

activity of the OB/ODD domain is not well characterised, but is thought to be an important regulatory domain that licences TPase domain function through interaction with LpoA (Sardis et al. 2021). The relative peptidoglycan density and UPLC traces are shown (Supp. Fig. 19).

In addition, we studied how the Δ*mreB* and *pbp1A* OB/ODD and TP domain mutations affect the location of active cell wall synthesis. This was achieved by incorporation of fluorescently labelled D-amino acids (FDAAs) via brief pulses of BADA into exponentially growing cells followed by microscopy to visualise locations of active cell wall synthesis (Fig. 4C and Supp. Fig. 21). In SBW25, BADA incorporation into the cell wall was homogeneous across the lateral surface during growth, but enriched at the mid-cell during septation. In SBW25 Δ*mreB* cells, BADA labelling was heterogeneous across the entire cell wall. This is contrary to expectation – at odds with observations of diffuse and homogeneous wall synthesis in MreB-depleted *E. coli* (Ursell et al. 2014) – and indicates that even in the absence of MreB, cell wall synthesis is active. SBW25 Δ*mreB* containing *pbp1A** mutations resulted in small spherical cells in which the prominence of cell wall synthesis in the septal region was restored as the primary location of peptidoglycan production, particularly in longer cells (Fig. 4C). Thus *pbp1A* mutations appear to restore cell homogeneity by eliminating disorganised patterns of cell wall synthesis (Fig. 4C).

Discussion

Ability to generate a viable *mreB* deletion mutant of *P. fluorescens* SBW25 – albeit with significantly compromised fitness – has provided opportunity to investigate the phenotypic consequences of loss of MreB function without use of MreB-inhibiting drugs, and to explore mutational routes leading to fitness restoration.

After 250 generations of selection, fitness of all derived lines was restored to wild type levels (Fig. 2A). Measurement of fitness at earlier time points showed that compensation occurred early in the selection regime and in single steps (Fig 2A, Supp. Fig. 8), consistent with compensation occurring via one or a small number of mutations. Sequencing and genetic reconstruction experiments confirmed, particularly for the class of mutant with defects in *pbp1A*, that single point mutations reducing or eliminating gene function were sufficient. In all derived lines, cell shape remained spherical. This sits in accord with evidence suggesting that there are no genetic routes or growth conditions able to restore rod-like shape in the absence of MreB (Shi et al. 2018). This stated, we recognise that rod-shape bacteria belonging to the *Actinobacteria* and *Rhizobiales* lack MreB (Margolin 2009; Zhao et al. 2021) suggesting that in principle it is possible to restore rod-shape in the absence of MreB.

In experiments where selection is used to find mutations that compensate for deleterious effects arising from deletion of a gene that compromises fitness (Laan et al. 2015; Lind et al. 2015; Rainey et al. 2017), a central issue concerns the focus of selection: the defect that selection might stand to correct. In this work, where deletion of *mreB* provided the compromised starting genotype, the most obvious difference between SBW25 Δ*mreB* and each of the ten derived lines was cell volume. It is therefore tempting to suggest that volume is a target of selection, and especially so given known adaptive changes in cell volume in the long-term Lenski experiment (Lenski and Travisano 1994; Monds et al. 2014). However, a closer examination of data, particularly from time-resolved microscopy, patterns of peptidoglycan synthesis and biophysical considerations, suggests a more complex set of effects and adaptive responses.

At first glance, the most notable distinction between cells of ancestral and derived types was shape and volume: SBW25 cells are rod shaped (thus with low compactness) with relatively little variance in the volume of daughter cells, whereas the shape of Δ*mreB* cells tends

toward spherical with large variance in volume. While the rate of elongation is the same in SBW25 and Δ*mreB* cells, substantial variance was apparent in the rate of elongation among daughter (Δ*mreB*) cells (Fig. 1D). Also evident were significant differences in cell viability, with viability of daughter cells being high in SBW25, but much reduced in the Δ*mreB* mutant. With focus on Δ*mreB* cells, viability of daughter cells depends on cell volume and declines significantly in both very large and very small cells (Fig. 1G). This is understandable in terms of effects on DNA segregation, with small cells proving non-viable most likely through lack of DNA, and large cells being similarly non-viable as a consequence of multiple copies of intertwined chromosomes and imbalance of osmotic pressure.

A key issue concerns the causes of variability in cell volume, toward which both septation asymmetry (C_s) and differential elongation rate (C_g) between daughter cells are the primary contributory factors. As evident by comparing C_s and C_g for ancestral SBW25 (black open square in Figs 3C and 3D) and Δ*mreB* (blue open circle in Figs 3C and 3D) cells, respectively, the greatest difference is the relative difference in elongation rate among sister cells (C_g). This indicates that this is the primary cause of variability in cell volume in the *mreB* mutant. Moreover, if correct, it leads to the prediction that fitness restoration will depend on selection finding mutational routes to restore population-level homogeneity in elongation rate among offspring.

What then, underlies differences in elongation rate? Here, data on peptidoglycan cross-linking, TPase activity, and patterns of cell wall synthesis in SBW25 versus Δ*mreB* cells are suggestive. Relative to SBW25, cells of the *mreB* mutant showed increased peptidoglycan cross-linking (Fig. 4A) likely resulting from enhanced TPase activity of Pbp1A (Fig. 4B) and heterogeneous (uneven) patterns of cell wall synthesis (Fig. 4C). These data indicate that despite the absence of MreB, cell wall synthesis continues, but is dysregulated in space and time. This is in marked contrast to cell wall synthesis in MreB-impaired (by treatment with A22) *E. coli* where cell wall synthesis is diffuse and homogeneous (Ursell et al. 2014).

Just what contributes to cell wall synthesis on removal of MreB is unclear. The standard view is that on deletion (or depolymerisation) of MreB, the elongasome is registered non-functional (Park and Uehara 2008), but compelling evidence appears to be lacking (Cho et al. 2016). In *E. coli*, PBP2 can trigger elongasome initiation independently of MreB by

promoting interaction with a hypothetical protein that in turn interacts with PBP2 and the cell wall (Özbaykal et al. 2020). Additionally, in *A. baumannii* high Pbp1A activity inhibits elongasome function (Simpson et al. 2021) with Δ*ponA* (*pbp1A*) mutants having enhanced elongasome function (Kang et al. 2021). Accordingly, in the following discussion we present two hypotheses to account for our findings: the first assumes that the elongasome is non-functional, whereas the second considers the possibility that the elongasome remains functional, but is stalled (or trapped).

Irrespective of whether the elongasome is rendered non-functional on removal of MreB, it is necessary to explain the observed heterogeneity of cell wall synthesis. Assuming, firstly, a non-functional elongasome, then obvious candidates for cell wall synthesis are the aPBPs, Pbp1A and Pbp1B, that can function independently of the elongasome (Cho et al. 2016) (although depend on activation by LpoA and LpoB respectively), with Pbp1B being particularly important in repair of cell wall lesions (Vigouroux et al. 2020). Perhaps heterogeneity of cell wall synthesis in Δ*mreB* arises from attempts by Pbp1B to repair large scale lesions, but there being insufficient bound (active) Pbp1B to fully accomplish this.

Assuming that the peptidoglycan-synthesising activity of the elongasome remains active on deletion of *mreB*, then heterogeneity of cell wall synthesis indicates that the multi-protein complex has become either stalled or trapped. This is reminiscent of observations in *B. subtilis* where inactivation of MreB causes failure in the dynamic redistribution of PBP1 (Kawai et al. 2009). Stalling – and concomitant heterogeneity of synthesis – could arise from elevated TPase activity that could in turn stem from altered interactions between Pbp2 and Pbp1A, which are known to mutually affect the catalytic activity of the other (Banzhaf et al. 2012; Egan et al. 2020). In support of this hypothesis, the TPase activity of Pbp1A in SBW25 Δ*mreB* is elevated compared to the same protein in ancestral SBW25 (Fig. 4B).

In the populations derived from the 1,000 generation selection experiment, solutions to variability in cell volume stemmed largely from reduction (or complete abolition) of Pbp1A function. As predicted above and shown in Fig. 3D, derived lines showed greatest improvement in the degree to which daughter cells differ in elongation rate (C_g). Such improvement correlates directly with significant increases in the probability that daughter cells are viable. By way of comparison changes in the relative positioning of the septum among daughter cells in derived lines (C_s) were relatively minor. Selection thus appears to

have restored fitness by changes that reduced variation in the rate of elongation among daughter cells. Assays of TPase and peptidoglycan cross-linking indicate that this is linked to reduction of TPase function of Pbp1A and a reduction in peptidoglycan cross-linking, with the two together likely favouring a disorganised cell wall architecture suited to the topology of spherical cells (Fig. 4D)

That selection compensated for the maladapted effects of *mreB* deletion by mutations in *pbp1A* can now be viewed in light of the two hypotheses for heterogeneity in cell wall synthesis. In the case of heterogeneity stemming from absence of elongasome function and localised activity of Pbp1B – and drawing upon the findings that inactivation of Pbp1A in *E. coli* results in a four-fold elevation of the amount of bound (and thus active) Pbp1B (Vigouroux et al. 2020) – inactivation of Pbp1A is expected to significantly increase Pbp1B activity perhaps to a level that would allow for wall repair uniformly throughout the cell (Vigouroux et al. 2020). Should heterogeneity in cell wall synthesis arise from a stalled, but otherwise functional elongasome, then elimination of Pbp1A might serve to correct the balance between TPase and GTase activity and thus allow the elongasome to move more diffusively along the inner membrane (Simpson et al. 2021). Future work is planned to test these competing hypotheses aided by the fact that deletion of *mreB* in SBW25 is not lethal.

The reason that compromised, albeit viable Δ*mreB* cells, can be generated in SBW25 under standard laboratory conditions is unknown, but answers may shed new light on the complexities of elongasome function and particularly the connection between elongasome function and MreB. Deletion of *mreB* in many bacteria is lethal including the closely related *P. aeruginosa* (Robertson et al. 2007), although in *E. coli* the defect can be rescued by slow growth or by increased activity of the cell division protein FtsZ (Kruse et al. 2005; Bendezú and de Boer 2008). In *B. subtilis* lethality can be ameliorated by growth in the presence of magnesium (Formstone and Errington 2005). This suggests that factors contributing to lethality involve subtleties in interactions among elongasome components (including associated factors such as *pbp1A* and *pbp1B*), which are dysregulated in SBW25 Δ*mreB*, but are insufficiently out of kilter to result in a lethal phenotype.

In this context there exists possible explanations for the repeated and independent transitions from ancestral rod-shape cells to cocci (Siefert and Fox 1998). Recent work on the rod to coccus transition in nasopharyngeal pathogens of the *Neisseriaceae* family, where deletion of

mreB and other determinants of the Rod complex, while not lethal, result in a significant fitness decrease (Veyrier et al. 2015). Such reductions in fitness were not apparent when coccoid cells arose from deletion of the FtsZ ring assembly-promoting protein YacF (ZapD), suggesting the requirement for a series of events beginning with loss of *yacF* followed by evolutionary compensation with eventual loss of the elongasome machinery (Veyrier et al. 2015). Our work here shows that the evolutionary route from rod to sphere is readily achievable under laboratory conditions via loss of *mreB* followed by compensatory mutation in *pbp1A* and reorganisation of peptidoglycan structure. Whether such a route is ever realised in nature will depend on the initial fitness effects of the *mreB* mutation, which in turn will depend on environmental context, but it is not implausible that inactivation of *mreB* may confer a fitness advantage under some conditions. This argument is further elaborated by Yulo and Hendrickson (2019).

Given the complexity of the cell wall synthesis machinery that defines rod-shape in bacteria, it is hard to imagine how rods could have evolved prior to cocci. However, the cylindrical shape offers a number of advantages. For a given biomass (or cell volume), shape determines surface area of the cell envelope, which is the smallest surface area associated with the spherical shape. As shape sets the surface/volume ratio, it also determines the ratio between supply (proportional to the surface) and demand (proportional to cell volume). From this point of view, it is more efficient to be cylindrical (Young 2006). This also holds for surface attachment and biofilm formation (Young 2006). But above all, for growing cells, the ratio between supply and demand is constant in rod shaped bacteria, whereas it decreases for cocci. This requires that spherical cells evolve complex regulatory networks capable of maintaining the correct concentration of cellular proteins despite changes in surface/volume ratio. From this point of view, rod-shaped bacteria offer opportunities to develop unsophisticated regulatory networks.

While fitness in the majority of experimental lines was restored by mutations in *pbp1A*, one line, Line 5, contained a mutation in *ftsZ*, but oddly this mutation, while apparent at generation 500, was undetected by population sequencing at generation 1,000 (Supp Table 1). Interestingly, the FtsZ D176A mutation occurred at precisely the same position as was found in a separate selection experiment in which compensatory mutations ameliorating harmful fitness effects associated with deletion of *rodA* were sought (D. W. Rogers, E. Franceschini & P. B. Rainey, unpublished). The prevalence of *pbp1A* mutations in the work

reported here likely reflects the fact that loss-of-function mutations in *pbp1A* are more readily achieved compared to gain-of-function mutations in *ftsZ*. This is evident in screening of mutations in *pbp1A* at generation 50, where all lines carried at least one *pbp1A* mutation (Supp Table 2). It will be of interest to determine whether *ftsZ* mutations that restore fitness to Δ*rodA* cells also compensate for defects due to elimination of *mreB*.

Derived Line 7, which carries a five gene deletion spanning the outer membrane porin OprD – and with the possibility of additional effects via mutation in *ftsE* – provides a contrasting route for compensatory evolution. Although *oprD* has not been specifically deleted, it seems reasonable to predict that in the absence of the porin, influx of water is likely limited, thus damping changes in turgor pressure and reducing cell swelling. Curiously, deletion of the focal five genes from SBW25 led to incomplete septation (Fig. 4C and Supp. Fig. 15F), with an indication from time-resolved movies of Δ*mreB* ΔPFLU4921-4925 (Supp. Movie 3) that there is also fault with septation in this background. This suggests that while ΔPFLU4921-4925 contributed to rescue of Δ*mreB*, it came at a cost to septum formation, which was subsequently rescued by mutation in the transmembrane divisome protein FtsE.

In conclusion, we return to the possibilities for new understanding of complex cellular processes arising from use of natural selection to rescue genetically perturbed cells (Lind et al. 2019; Remigi et al. 2019; LaBar et al. 2020). Here, a fitness-compromised, but viable, *mreB* deletion mutant of *P. fluorescens* SBW25 provided opportunity to explore consequences of both the initial genetic lesion and the bases of fitness compensation. In part attributable to the fact that Δ*mreB* SBW25 is viable, it was possible to glimpse functional effects arising from deletion of MreB, namely, uneven rates of growth among daughter cells caused by heterogeneity in patterns of cell wall synthesis. Restoration of fitness was readily achieved by mutations that reduced (or eliminated) Pbp1A function or increased septation. The primary effect was to reduce variance in growth rate among daughter cells, which is connected to resumption in homogeneity of cell wall synthesis. Disentangling two explanatory hypotheses – one invoking a role for Pbp1B and the other that elongasome function in SBW25 depends on a correct balance of among cell wall synthesising enzymes – awaits future work.

Acknowledgements

We thank Olin Silander for helpful discussions and for his assistance to PRY with principal components analysis of cell shape, Sebastian Schmeier and Saumya Agrawal for bioinformatic analyses, Dave Rogers for valuable discussion, and both Dave Rogers and Tim Cooper for comments on the manuscript. PBR is especially grateful to Malavika Venu, Norma Rivera and Dave Rogers who made the Δ*mreB* Δ*pbp1A* mutant and Ellen McConnell who introduced fluorescent markers and measured fitness effects. Electron Microscopy was provided by Massey University and was performed by Niki Murray, Manawatu Microscopy and Imaging Centre, Massey University, Palmerston North, NZ. PBR thanks the Royal Society of New Zealand (James Cook Fellowship) and acknowledges generous core support from the Max Planck Society. Research in the Cava lab was supported by the Swedish Research Council (2018-02823 and 2018-05882), Umeå University, the Knut and Alice Wallenberg Foundation and the Kempe Foundation (SMK2062). Open access funding is provided by the Max Planck Society. PBR dedicates the paper to the memory of Andrew Spiers, colleague and ardent wrinkliologist, whose 2002 manuscript first reported the fact that a transposon insertion in *mreB* abolishes wrinkly morphology, but not viability.

Author contributions

PRY: Construction of SBW25 GFP, phase contrast and fluorescence (BADA) microscopy, flow cytometry, growth assays, data collection, protein modelling, manuscript review. ND: microscopy, data collection / analysis, manuscript preparation. MG: Construction of SBW25 Δ*mreB*, selection experiment and fitness measures, manuscript review. BRR: Peptidoglycan analysis, Bocillin-FL PBP labelling assays, data analysis and manuscript review. ADF: Sequencing and data analysis, manuscript review. XXZ & YH: Genetics and mutation construction, manuscript review. MM: Mutation construction, aztreonam analysis. FC: Supervision, funding acquisition, data analysis, manuscript review. PBR: Experimental conception and design, funding acquisition, microscopy, data analysis, manuscript preparation. HH: DNA extraction and sequencing, supervision of PRY, manuscript preparation.

References

Banzhaf M, van den Berg van Saparoea B, Terrak M, Fraipont C, Egan A, Philippe J, Zapun A, Breukink E, Nguyen-Distèche M, den Blaauwen T, et al. 2012. Cooperativity of peptidoglycan synthases active in bacterial cell elongation. *Mol. Microbiol.* 85:179–194.

Bendezú FO, de Boer PAJ. 2008. Conditional lethality, division defects, membrane involution, and endocytosis in *mre* and *mrd* shape mutants of *Escherichia coli*. *J. Bacteriol.* 190:1792–1811.

Bertsche U, Kast T, Wolf B, Fraipont C, Aarsman MEG, Kannenberg K, Von Rechenberg M, Nguyen-Distèche M, Den Blaauwen T, Höltje J-V, et al. 2006. Interaction between two murein (peptidoglycan) synthases, PBP3 and PBP1B, in *Escherichia coli*. *Mol. Microbiol.* 61:675–690.

Campos M, Surovtsev IV, Kato S, Paintdakhi A, Beltran B, Ebmeier SE, Jacobs-Wagner C. 2014. A constant size extension drives bacterial cell size homeostasis. *Cell* 159:1433–1446.

Cho H, Wivagg CN, Kapoor M, Barry Z, Rohs PDA, Suh H, Marto JA, Garner EC, Bernhardt TG. 2016. Bacterial cell wall biogenesis is mediated by SEDS and PBP polymerase families functioning semi-autonomously. *Nat. Microbiol.* 1:16172.

Claessen D, Emmins R, Hamoen LW, Daniel RA, Errington J, Edwards DH. 2008. Control of the cell elongation-division cycle by shuttling of PBP1 protein in *Bacillus subtilis*. *Mol. Microbiol.* 68:1029–1046.

Daniel RA, Errington J. 2003. Control of cell morphogenesis in bacteria: two distinct ways to make a rod-shaped cell. *Cell* 113:767–776.

Deatherage DE, Barrick JE. 2014. Identification of mutations in laboratory-evolved microbes from next-generation sequencing data using breseq. *Methods Mol. Biol.* 1151:165–188.

Desmarais SM, De Pedro MA, Cava F, Huang KC. 2013. Peptidoglycan at its peaks: how chromatographic analyses can reveal bacterial cell-wall structure and assembly. *Mol. Microbiol.* 89:1–13.

Egan AJF, Errington J, Vollmer W. 2020. Regulation of peptidoglycan synthesis and remodelling. *Nat. Rev. Microbiol.* 18:446–460.

Errington J. 2003. Regulation of endospore formation in *Bacillus subtilis*. *Nat. Rev. Microbiol.* 1:117–126.

Formstone A, Errington J. 2005. A magnesium-dependent *mreB* null mutant: implications for the role of *mreB* in *Bacillus subtilis*. *Mol. Microbiol.* 55:1646–1657.

Geisinger E, Mortman NJ, Dai Y, Cokol M, Syal S, Farinha A, Fisher DG, Tang AY, Lazinski DW, Wood S, et al. 2020. Antibiotic susceptibility signatures identify potential antimicrobial targets in the Acinetobacter baumannii cell envelope. *Nat. Commun.* 11:4522.

Hsu Y-P, Rittichier J, Kuru E, Yablonowski J, Pasciak E, Tekkam S, Hall E, Murphy B, Lee TK, Garner EC, et al. 2017. Full color palette of fluorescent D-amino acids for in situ labeling of bacterial cell walls. *Chem. Sci.* 8:6313–6321.

Huang KC, Mukhopadhyay R, Wen B, Gitai Z, Wingreen NS. 2008. Cell shape and cell-wall organization in Gram-negative bacteria. *Proc. Natl. Acad. Sci. U. S. A.* 105:19282–19287.

Humphrey W, Dalke A, Schulten K. 1996. VMD: visual molecular dynamics. *J. Mol. Graph.* 14:33–38, 27–28.

Ishino F, Park W, Tomioka S, Tamaki S, Takase I, Kunugita K, Matsuzawa H, Asoh

S, Ohta T, Spratt BG. 1986. Peptidoglycan synthetic activities in membranes of *Escherichia coli* caused by overproduction of penicillin-binding protein 2 and *rodA* protein. *J. Biol. Chem.* 261:7024–7031.
Iwai N, Nagai K, Wachi M. 2002. Novel *S*-Benzylisothiourea compound that induces spherical cells in *Escherichia coli* probably by acting on a rod-shape-determining protein(s) other than penicillin-binding protein 2. *Biosci. Biotechnol. Biochem.* 66:2658–2662.
Job V, Carapito R, Vernet T, Dessen A, Zapun A. 2008. Common alterations in PBP1a from resistant *Streptococcus pneumoniae* decrease its reactivity toward beta-lactams: structural insights. *J. Biol. Chem.* 283:4886–4894.
Julou T, Mora T, Guillon L, Croquette V, Schalk IJ, Bensimon D, Desprat N. 2013. Cell-cell contacts confine public goods diffusion inside *Pseudomonas aeruginosa* clonal microcolonies. *Proc. Natl. Acad. Sci. U. S. A.* 110:12577–12582.
Jun S, Mulder B. 2006. Entropy-driven spatial organization of highly confined polymers: lessons for the bacterial chromosome. *Proc. Natl. Acad. Sci. U. S. A.* 103:12388–12393.
Jun S, Wright A. 2010. Entropy as the driver of chromosome segregation. *Nat. Rev. Microbiol.* 8:600–607.
Kang KN, Boll JM. 2022. PBP1A directly interacts with the divisome complex to promote septal peptidoglycan synthesis in *Acinetobacter baumannii*. *J. Bacteriol.* 204:e00239-22.
Kang KN, Kazi MI, Biboy J, Gray J, Bovermann H, Ausman J, Boutte CC, Vollmer W, Boll JM. 2021. Septal class A penicillin-binding protein activity and ld-transpeptidases mediate selection of colistin-resistant lipooligosaccharide-deficient *Acinetobacter baumannii*. *mBio* 12:e02185-20.
Kawai Y, Daniel RA, Errington J. 2009. Regulation of cell wall morphogenesis in *Bacillus subtilis* by recruitment of PBP1 to the MreB helix. *Mol. Microbiol.* 71:1131–1144.
Kruse T, Bork-Jensen J, Gerdes K. 2005. The morphogenetic MreBCD proteins of *Escherichia coli* form an essential membrane-bound complex. *Mol. Microbiol.* 55:78–89.
Kumar S, Stecher G, Tamura K. 2016. MEGA7: Molecular evolutionary genetics analysis version 7.0 for bigger datasets. *Mol. Biol. Evol.* 33:1870–1874.
Laan L, Koschwanez JH, Murray AW. 2015. Evolutionary adaptation after crippling cell polarization follows reproducible trajectories. *eLife* 4:e09638.
LaBar T, Phoebe Hsieh Y-Y, Fumasoni M, Murray AW. 2020. Evolutionary repair experiments as a window to the molecular diversity of life. *Curr. Biol.* 30:R565–R574.
Land AD, Winkler ME. 2011. The requirement for pneumococcal MreC and MreD is relieved by inactivation of the gene encoding PBP1a. *J. Bacteriol.* 193:4166–4179.
Lenski RE, Travisano M. 1994. Dynamics of adaptation and diversification: a 10,000-generation experiment with bacterial populations. *Proc. Natl. Acad. Sci.* 91:6808–6814.
Lind PA, Farr AD, Rainey PB. 2015. Experimental evolution reveals hidden diversity in evolutionary pathways. *eLife* 4:e07074.
Lind PA, Farr AD, Rainey PB. 2017. Evolutionary convergence in experimental Pseudomonas populations. *ISME J.* 11:589–600.
Lind PA, Libby E, Herzog J, Rainey PB. 2019. Predicting mutational routes to new

adaptive phenotypes. *eLife* 8:e38822.
Liu J, Dazzo FB, Glagoleva O, Yu B, Jain AK. 2001. CMEIAS: A Computer-Aided System for the Image Analysis of Bacterial Morphotypes in Microbial Communities. *Microb. Ecol.* 41:173–194.
Liu Y, Rainey PB, Zhang X-X. 2014. Mini-Tn7 vectors for studying post-transcriptional gene expression in *Pseudomonas*. *J. Microbiol. Methods* 107:182–185.
Locke JCW, Elowitz MB. 2009. Using movies to analyse gene circuit dynamics in single cells. *Nat. Rev. Microbiol.* 7:383–392.
Mallik S, Dodia H, Ghosh A, Srinivasan R, Good L, Raghav SK, Beuria TK. 2023. FtsE, the nucleotide binding domain of the ABC transporter homolog FtsEX, regulates septal PG synthesis in *E. coli*. *Microbiol. Spectr.* 11:e0286322.
Margolin W. 2009. Sculpting the bacterial cell. *Curr. Biol.* 19:R812-822.
Monds RD, Lee TK, Colavin A, Ursell T, Quan S, Cooper TF, Huang KC. 2014. Systematic perturbation of cytoskeletal function reveals a linear scaling relationship between cell geometry and fitness. *Cell Rep.* 9:1528–1537.
Murray T, Popham DL, Setlow P. 1998. *Bacillus subtilis* cells lacking penicillin-binding protein 1 require increased levels of divalent cations for growth. *J. Bacteriol.* 180:4555–4563.
Näsvall J, Sun L, Roth JR, Andersson DI. 2012. Real-time evolution of new genes by innovation, amplification, and divergence. *Science* 338:384–387.
Osborn MJ, Rothfield L. 2007. Cell shape determination in *Escherichia coli*. *Curr. Opin. Microbiol.* 10:606–610.
Özbaykal G, Wollrab E, Simon F, Vigouroux A, Cordier B, Aristov A, Chaze T, Matondo M, van Teeffelen S. 2020. The transpeptidase PBP2 governs initial localization and activity of the major cell-wall synthesis machinery in E. coli. *eLife* 9:e50629.
Park JT, Uehara T. 2008. How bacteria consume their own exoskeletons (turnover and recycling of cell wall peptidoglycan). *Microbiol. Mol. Biol. Rev.* 72:211–227.
Patel Y, Zhao H, Helmann JD. 2020. A regulatory pathway that selectively up-regulates elongasome function in the absence of class A PBPs. *eLife* 9:e57902.
Pinho MG, Kjos M, Veening J-W. 2013. How to get (a)round: mechanisms controlling growth and division of coccoid bacteria. *Nat. Rev. Microbiol.* 11:601–614.
Rainey PB, Remigi P, Farr AD, Lind PA. 2017. Darwin was right: where now for experimental evolution? *Curr. Opin. Genet. Dev.* 47:102–109.
Randich AM, Brun YV. 2015. Molecular mechanisms for the evolution of bacterial morphologies and growth modes. *Front. Microbiol.* 6:580.
Remigi P, Capela D, Clerissi C, Tasse L, Torchet R, Bouchez O, Batut J, Cruveiller S, Rocha EPC, Masson-Boivin C. 2014. Transient hypermutagenesis accelerates the evolution of legume endosymbionts following horizontal gene transfer. *PLOS Biol.* 12:e1001942.
Remigi P, Masson-Boivin C, Rocha EPC. 2019. Experimental evolution as a tool to investigate natural processes and molecular functions. *Trends Microbiol.* 27:623–634.
Robert X, Gouet P. 2014. Deciphering key features in protein structures with the new ENDscript server. *Nucleic Acids Res.* 42:W320-324.
Robertson GT, Doyle TB, Du Q, Duncan L, Mdluli KE, Lynch AS. 2007. A Novel indole compound that inhibits *Pseudomonas aeruginosa* growth by targeting

MreB is a substrate for MexAB-OprM. *J. Bacteriol.* 189:6870–6881.
Rojas ER, Huang KC. 2018. Regulation of microbial growth by turgor pressure. *Curr. Opin. Microbiol.* 42:62–70.
Sardis MF, Bohrhunter JL, Greene NG, Bernhardt TG. 2021. The LpoA activator is required to stimulate the peptidoglycan polymerase activity of its cognate cell wall synthase PBP1a. *Proc. Natl. Acad. Sci. U. S. A.* 118:e2108894118.
Shi H, Bratton BP, Gitai Z, Huang KC. 2018. How to build a bacterial cell: MreB as the foreman of *E. coli* construction. *Cell* 172:1294–1305.
Siefert't JL, Fox GE. 1998. Phylogenetic mapping of bacterial morphology. *Microbiol.* 144:2803–2808.
Simpson BW, Nieckarz M, Pinedo V, McLean AB, Cava F, Trent MS. 2021. *Acinetobacter baumannii* can survive with an outer membrane lacking lipooligosaccharide due to structural support from elongasome peptidoglycan synthesis. *mBio* 12:e0309921.
Skurnik D, Roux D, Cattoir V, Danilchanka O, Lu X, Yoder-Himes DR, Han K, Guillard T, Jiang D, Gaultier C, et al. 2013. Enhanced *in vivo* fitness of carbapenem-resistant *oprD* mutants of *Pseudomonas aeruginosa* revealed through high-throughput sequencing. *Proc. Natl. Acad. Sci. U. S. A.* 110:20747–20752.
Spiers AJ, Kahn SG, Bohannon J, Travisano M, Rainey PB. 2002. Adaptive divergence in experimental populations of *Pseudomonas fluorescens*. I. Genetic and phenotypic bases of wrinkly spreader fitness. *Genetics* 161:33–46.
Taheri-Araghi S, Bradde S, Sauls JT, Hill NS, Levin PA, Paulsson J, Vergassola M, Jun S. 2017. Cell-size control and homeostasis in bacteria. *Curr. Biol.* 27:1392.
van Teeffelen S, Renner LD. 2018. Recent advances in understanding how rod-like bacteria stably maintain their cell shapes. *F1000Research* 7:241.
Typas A, Banzhaf M, Gross CA, Vollmer W. 2012. From the regulation of peptidoglycan synthesis to bacterial growth and morphology. *Nat. Rev. Microbiol.* 10:123–136.
Ursell TS, Nguyen J, Monds RD, Colavin A, Billings G, Ouzounov N, Gitai Z, Shaevitz JW, Huang KC. 2014. Rod-like bacterial shape is maintained by feedback between cell curvature and cytoskeletal localization. *Proc. Natl. Acad. Sci. U. S. A.* 111:E1025-1034.
Verge-Serandour ML, Turlier H. 2021. A hydro-osmotic coarsening theory of biological cavity formation. *PLOS Comput. Biol.* 17:e1009333.
Veyrier FJ, Biais N, Morales P, Belkacem N, Guilhen C, Ranjeva S, Sismeiro O, Péhau-Arnaudet G, Rocha EP, Werts C, et al. 2015. Common cell shape evolution of two nasopharyngeal pathogens. *PLOS Genet.* 11:e1005338.
Vigouroux A, Cordier B, Aristov A, Alvarez L, Özbaykal G, Chaze T, Oldewurtel ER, Matondo M, Cava F, Bikard D, et al. 2020. Class-A penicillin binding proteins do not contribute to cell shape but repair cell-wall defects. *eLife* 9:e51998.
Winsor GL, Griffiths EJ, Lo R, Dhillon BK, Shay JA, Brinkman FSL. 2016. Enhanced annotations and features for comparing thousands of *Pseudomonas* genomes in the *Pseudomonas* genome database. *Nucleic Acids Res.* 44:D646-653.
Young KD. 2003. Bacterial shape. *Mol. Microbiol.* 49:571–580.
Young KD. 2006. The selective value of bacterial shape. *Microbiol. Mol. Biol. Rev.*

70:660–703.
Young KD. 2007. Bacterial morphology: why have different shapes? *Curr. Opin. Microbiol.* 10:596–600.
Young KD. 2010. Bacterial shape: two-dimensional questions and possibilities. *Annu. Rev. Microbiol.* 64:223–240.
Yousif SY, Broome-Smith JK, Spratt BG. 1985. Lysis of *Escherichia coli* by beta-lactam antibiotics: deletion analysis of the role of penicillin-binding proteins 1A and 1B. *J. Gen. Microbiol.* 131:2839–2845.
Yulo PRJ, Hendrickson HL. 2019. The evolution of spherical cell shape; progress and perspective. *Biochem. Soc. Trans.* 47:1621–1634.
Zhao W, Zhu H, Wei F, Zhou D, Li Y, Zhang X-X. 2021. Investigating the involvement of cytoskeletal proteins MreB and FtsZ in the origin of legume-rhizobial symbiosis. *Mol. Plant-Microbe Interact.* 34:547–559.

Figures

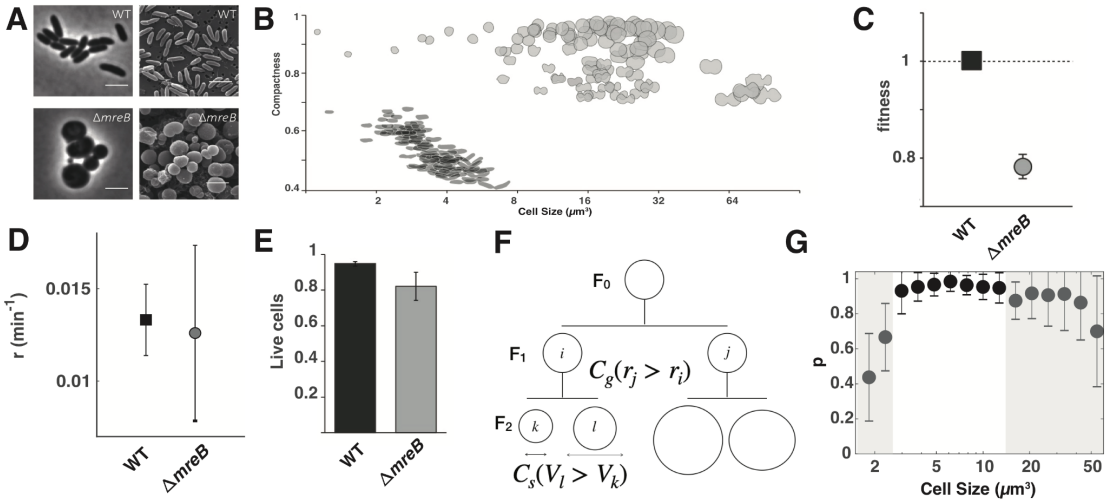

Figure 1. Characterisation of ancestral SBW25 and Δ*mreB* strains. Figure shows (A) photomicrographs of ancestral SBW25 and Δ*mreB*. Scale bars, 3 µm. B) The relationship between cell shape and estimated volume (V_e) is represented using compactness, a measure of roundness. One hundred representative cells from ancestral SBW25 and Δ*mreB* populations are shown as cell outlines. C) Fitness of ancestral SBW25 GFP and the Δ*mreB* mutant relative to ancestral SBW25 when both are in exponential phase during pairwise competition assays. Data are means and standard deviation of 50,000 cells each of ancestral SBW25 and Δ*mreB*, respectively, and 100,000 cells total, after competition. D) Elongation rate measured for SBW25 and Δ*mreB* SBW25. Error bars represent mean and standard deviation (N_{WT} = 94; $N_{\Delta mreB}$ = 99) E) Proportion of live cells in ancestral SBW25 (black bar) and ΔmreB (grey bar) based on LIVE/DEAD BacLight Bacterial Viability Kit protocol. Cells were pelleted at 2,000 x g for 2 minutes to preserve ΔmreB cell integrity. Error bars are means and standard deviation of three biological replicates (n>100). F) Schematic of asymmetric size production in cell lineages at generation F0 and F1. Asymmetries from differential growth rate between sister cells (*i,j*) are captured by C_g (see methods), while asymmetries in daughter (*l,k*) cell sizes at septation are measured by C_s. G) probability *p* to pass to the next generation as a function of cell size in Δ*mreB* cells. The shaded gray areas are indicative of regions where survival significantly drops.

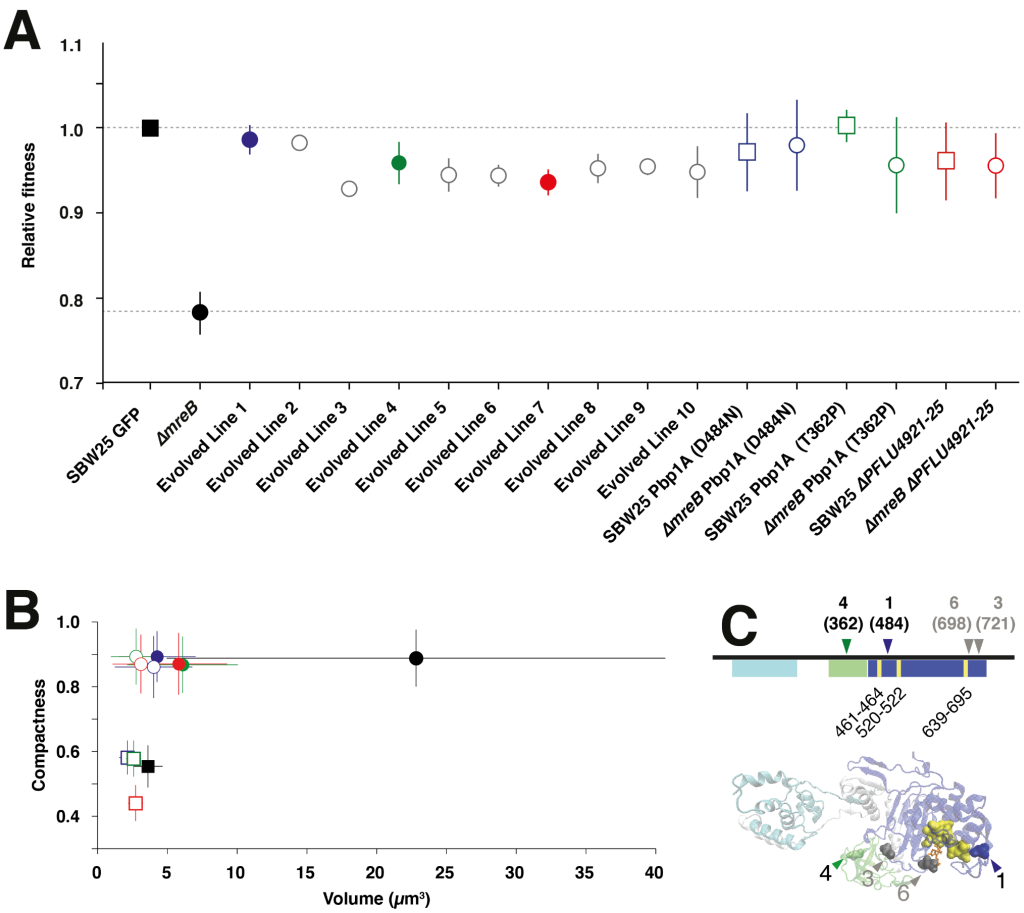

Figure 2. Characterisation of evolved lines at 1,000 generations. A) Relative fitness of the *ΔmreB* mutant, derived lines after ~1,000 generations, and mutant reconstructions in *ΔmreB* and SBW25, relative to SBW25 (dashed line) in pairwise competition experiments. Error bars represent standard deviation. B) Compactness versus estimated volume (Ve) of derived lines: Line 1 in blue, Line 4 in green and line 7 in red; derived mutations reconstructed in *ΔmreB*, and SBW25 backgrounds. Data points are means and SD of X 100 cells. Square data points represent rod-like cells, whereas circles (both open and filled) represent spherical cells. Ancestral genotypes are labeled in black. Open squares and open circles depict the reconstruction of mutations in the SBW25 and *ΔmreB* backgrounds, respectively. Filled circles represent the 1000 generation evolved lines from where the mutations have been identified. Colors as follows; blue is Line 1 or Pbp1A D484N, green is Line 4 or Pbp1A T362P, red is Line 7. C) Domain map and model of Pbp1A (PFLU0406) showing the 2 major domains; the glycosyltransferase (GT) domain (cyan) and the transpeptidase (TP) domain (blue). The oligonucleotide/oligosaccharide binding (OB) domain is shown in green. The active site of the TP domain is also shown (yellow). The locations of mutations from Lines 1 and 4 are indicated with coloured arrows in the *pbp1A* gene map and in the model of Pbp1A. The mutations in Lines 3 and 6 are also shown in grey but were not characterised further in this work.

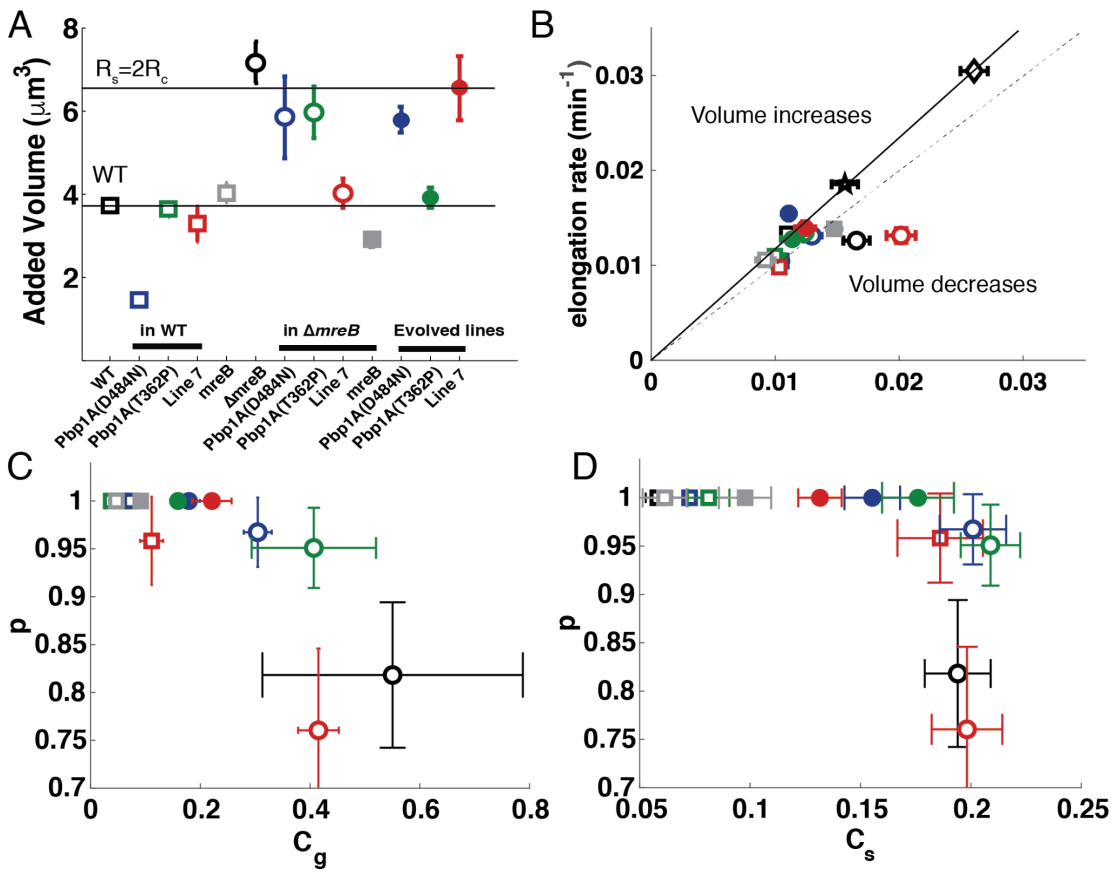

Figure 3. Cell size homeostasis: A) Average added volume for the different genotypes, which is cell volume at septation less cell volume at birth. The horizontal lines correspond to the volume of ancestral SBW25 cells and to their spherical counterparts (R_s=2*R_c). B) Elongation rate plotted against septation rate. The black line corresponds to size homeostasis of wild type strains (square = *P. fluorescens*; star = *P. aeruginosa*; diamond = *E. coli*). Below this line, septation is faster than elongation and cell size decreases. The dashed line corresponds to equal septation and elongation rates. C) The probability *p* to pass to the next generation as a function of growth asymmetry C_g. D) The probability *p* to pass to the next generation as a function of error in septum positioning measured as the relative cell size between daughters at division C_s. In A) B), C) and D) square data points (both open and filled) represent rod-like cells, whereas circles (both open and filled) represent spherical cells. Ancestral genotypes are labeled in black. Open squares and open circles depict the reconstruction of mutations in the WT and *ΔmreB* backgrounds, respectively. Filled circles represent the evolved lines where the mutations have been identified. Colors as in Fig 2; blue is Line 1 or Pbp1A D484N, green is Line 4 or Pbp1a T362P, red is Line 7, grey is ectopic *mreB* expression. Error bars represent standard errors. In A), B), D) : (N_{WT} = 94; N_{L1_WT} = 52 ; N_{L4_WT} = 38; N_{L7_WT} = 72; N_{mreB_WT} = 36; $N_{\Delta mreB}$ = 99; $N_{L1_\Delta mreB}$ = 92; $N_{L4_\Delta mreB}$ = 102; $N_{L7_\Delta mreB}$ = 96; $N_{mreB_\Delta mreB}$ = 64; N_{L1} = 88; N_{L4} = 74; N_{L7} = 76); in C) (N_{WT} = 47; N_{L1_WT} = 26 ; N_{L4_WT} = 19; N_{L7_WT} = 38; N_{mreB_WT} = 18; $N_{\Delta mreB}$ = 55; $N_{L1_\Delta mreB}$ = 56; $N_{L4_\Delta mreB}$ = 62; $N_{L7_\Delta mreB}$ = 53; $N_{mreB_\Delta mreB}$ = 32; N_{L1} = 44; N_{L4} = 42; N_{L7} = 40)

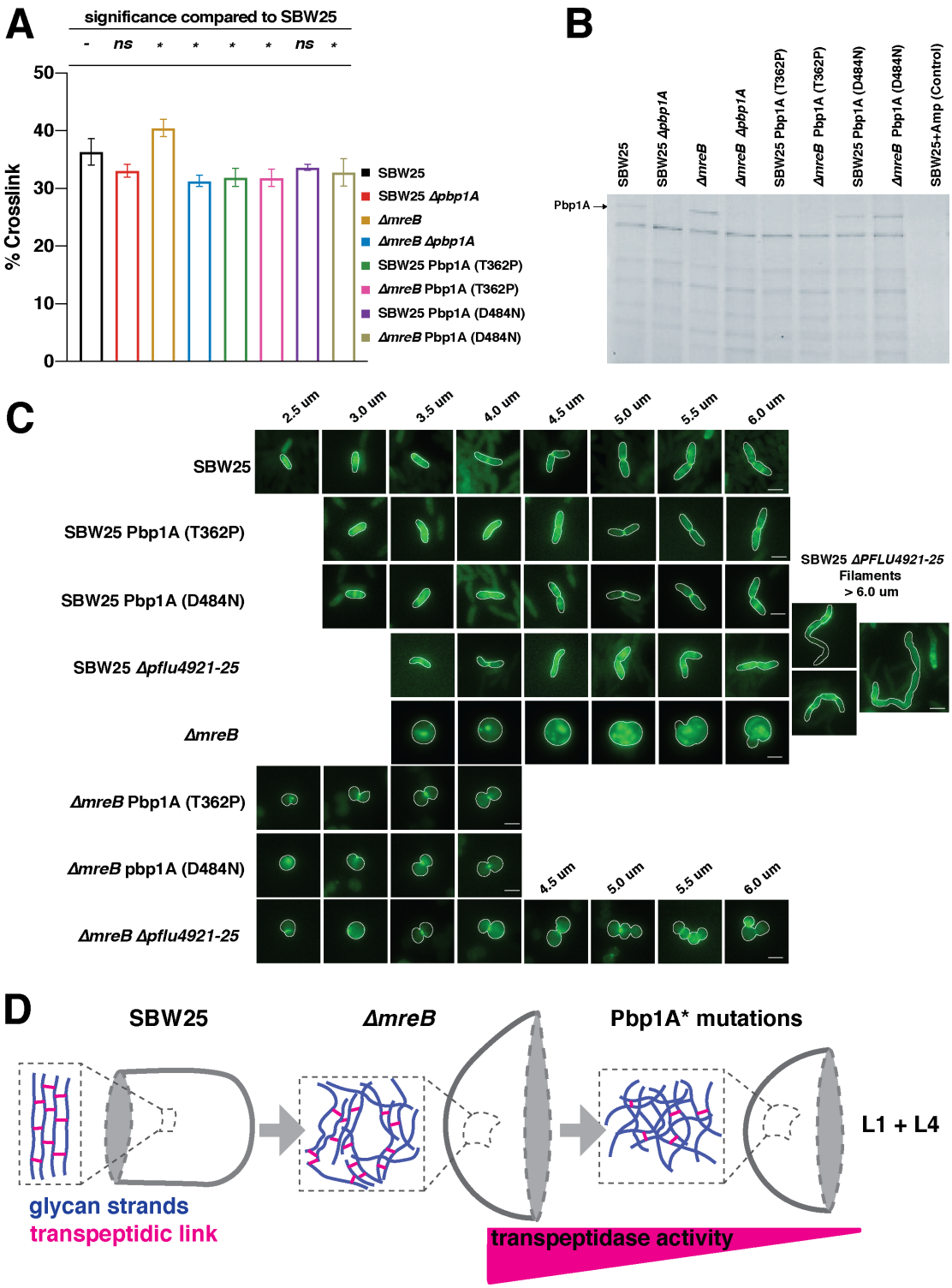

Figure 4. Molecular investigation of adaptive mutations in Δ*mreB* evolution. A) Peptidoglycan cross-linking in the cell walls of mutants in SBW25 and Δ*mreB* genetic backgrounds. The error bars (SD) are the result of 3 biological replicates. ANOVA revealed a highly significant difference among means [$F_{7,16}$ = 8.19, p < 0.001] with Dunnett's post-hoc test adjusted for multiple comparisons showing that five genotypes (*) differ significantly (p < 0.05) from SBW25. B) Cell extracts subjected to polyacrylamide gel and SDS PAGE labelling with Bocillin-FL gel to demonstrate penicillin binding of Pbp1A (labelled) and other Pbps in *P. fluorescens* SBW25. See Supp Fig 20 for quantification of band intensities. C) Fluorescent images of mutations in SBW25 and Δ*mreB* backgrounds subjected to short-pulse labelling with fluorescent D-amino acid BADA to reveal the location and organization of cell wall construction in the mutant backgrounds. As cells elongate in preparation to divide, septal peptidoglycan synthesis becomes more pronounced. Δ*mreB* cells have highly disorganized synthesis (see Supp.

Fig. 21 for quantitative analysis), which is alleviated in Δ*mreB* Pbp1A* and Δ*mreB* ΔPFLU4921-25 mutants. Cell outlines from phase contrast images show the cell boundaries. Scale bars = 2µm. D) Model of evolutionary rescue in Δ*mreB* mutant cells highlighting the organization of the predicted glycan meshwork in the rod and spherical geometries. In Pbp1A* mutants (Line 1 and Line 4), a decrease in transpeptidase activity favours disorganized cell wall architecture, which is better suited to the topology of a sphere.

Supplementary Material

Supplementary Table 1. Mutations identified in derived lines at generations 500 and 1,000.

	Mutation			
	Gene	Mutation	Freq @ 500	Freq @ 1,000
Line 1	*pbp1A*	D484N (GAT->AAT)	74% (n = 118)[1]	78% (n = 129)
Line 2	*ftsA*	H346R (CAC->CGC)	71% (n = 105)	72% (n = 114)
	ctpA	T174P (ACC->CCC)	66% (n = 93)	60% (n = 106)
Line 3	*pbp1A*	D721A (GAC->GCC)	99% (n = 75)	87% (n = 78)
Line 4	*pbp1A*	G719D (GGT->GAT)	60% (n = 90)	ND[2]
	pbp1A	T362P (ACC->CCC)	ND	98% (n = 100)
Line 5	*ftsZ*	D176A (GAC->GCC)	48% (n = 147)	ND
Line 6	*pbp1A*	N698K (AAC->AAG)	100% (n = 103)	100% (n = 52)
Line 7	deletion	5399934-5403214	30% (n = 34)	96% (n = 112)
	ftsE	T188A (ACC->GCC)	ND	63% (n = 125)
Line 8	*pbp1A*	del A at 450,515	39% (n = 94)	ND
	ctpA	T174P (ACC->CCC)	ND	73% (n = 105)
Line 9	*pbp1A*	G580D (GGC->GAC)	ND	42% (n = 86)
	pbp1A	W322* (TGG->TGA)	ND	40% (n = 111)
Line 10	*pbp1A*	T362P (ACC->CCC)	32% (n = 111)	ND
	pbp1A	G580D (GGC->GAC)	ND	36% (n = 100)

[1]Percentage of reads, n = number of reads.

[2]ND: no mutation detected.

Supplementary Table 2. Mutations in *pbp1A* at generation 50.

Line	Colonies with mutation (of 16 colonies)	Nucleotide position in PBP1a	Nucleotide change	Genomic Position	Protein-level change
1	16	1450	G>A	449754	D484N
2	1	2114	T>C	449090	F705S
2	1	1814 - 1815	Insertion	449389 - 449390	fs 605
3	3	1814 - 1815	Insertion	449389 - 449390	fs 605
4	2	1148 - 1149	Insertion	450055 - 450056	fs 383
4	1	1818 - 1819	Deletion	449385 - 449386	fs 606
6	4	2032	A>C	449172	T678P
6	1	1084	A>C	450120	T362P
7	1	922 - 923	Insertion	450281 - 450282	L308P
8	2	689	Deletion	450515	fs 230
8	1	1339	A>C	449865	S447R
9	2	996	A>G	450208	W>STOP
10	1	1739	G>A	449465	G580D

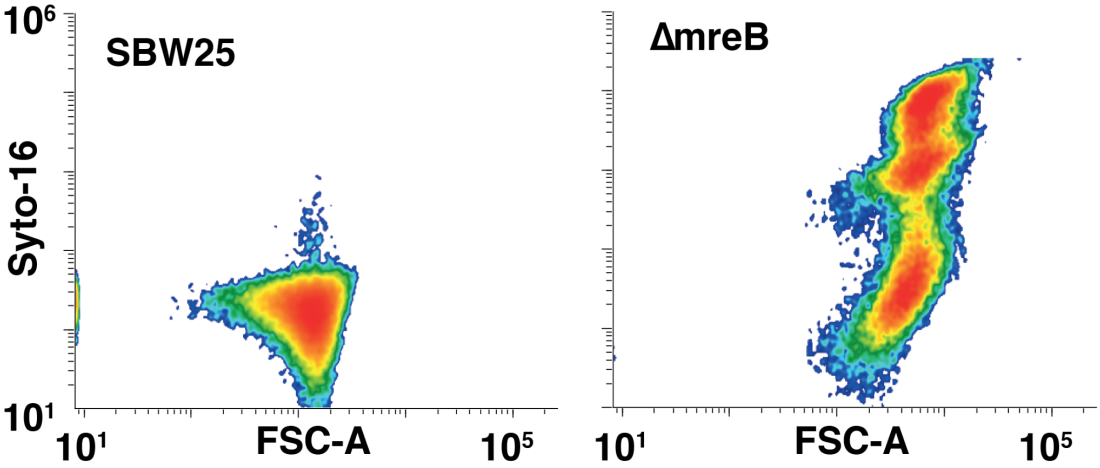

Supplementary Figure 1. Correlation between cell size and DNA content in SBW25 and Δ*mreB* cells. DNA per cell does not vary in SBW25 cells to the degree that it varies in the Δ*mreB* cells as they grow larger. Cells were stained with SYTO 16, a cell-permeant green-fluorescent nucleic acid stain, and analysed using flow cytometry (n = 50,000 events).

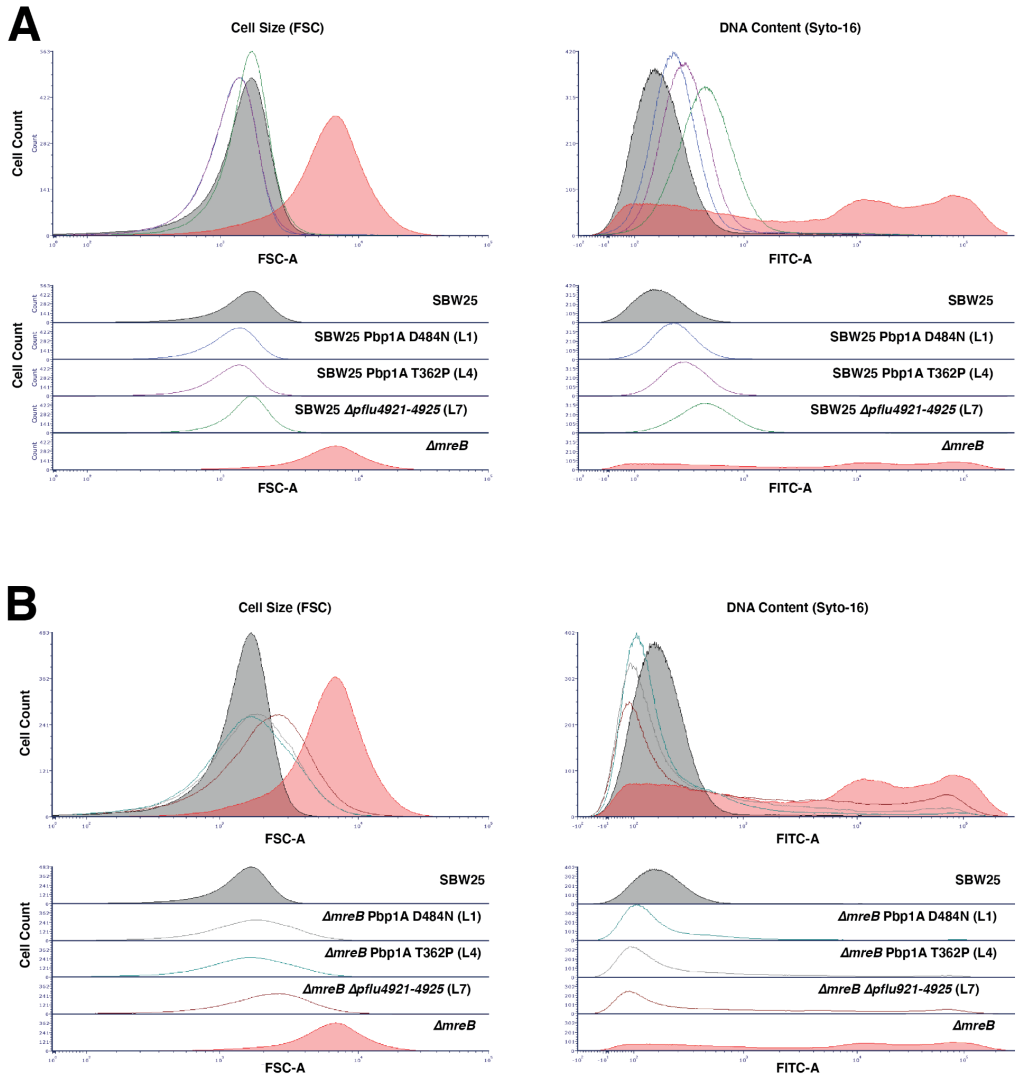

Supplementary Figure 2. Genomic content and cell size of cells with mutations of interest A) Flow cytometry reveals an increase in DNA content coupled with an increase in size of SBW25 Δ*mreB*. In the SBW25 background *pbp1A* Line 1 and Line 4 mutants are slightly smaller than SBW25 cells and have comparable DNA content. The Line 7 reconstruction cells are larger by FSC than SBW25 and contain more DNA, reflective of the filamenting phenotype seen via microscopy. B) In the Δ*mreB* background, all three reconstructions have smaller cells than Δ*mreB*, with DNA content that is similar to SBW25. A small proportion of cells with large amounts of DNA are seen in the Line 7 reconstruction; these are also observed via microscopy as clumped spherical cells forming incomplete septa.

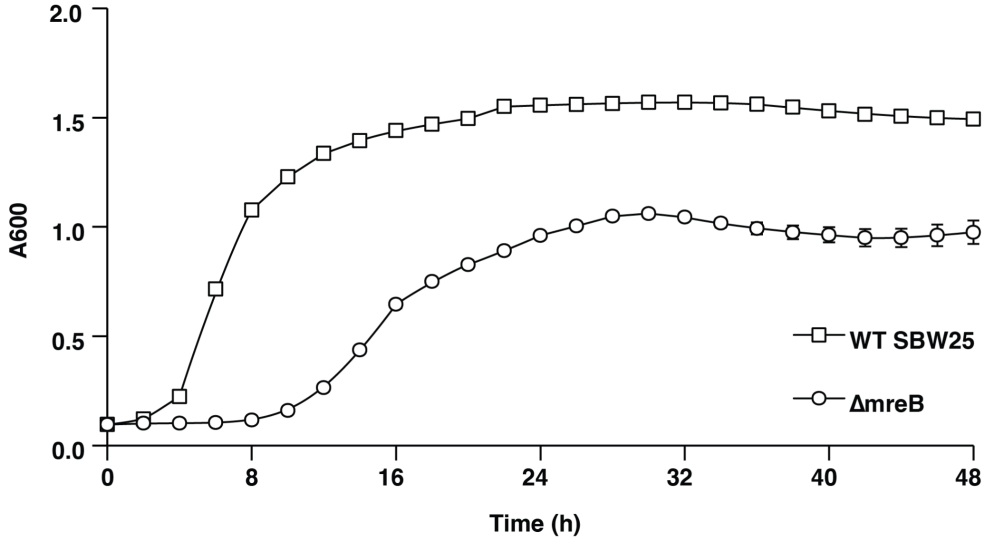

Supplementary Figure 3. Growth curves for ancestral SBW25 and Δ*mreB* strains as measured by OD 600 in LB. NB: All growth curves were produced simultaneously. Data are means and standard deviations of three biological replicates.

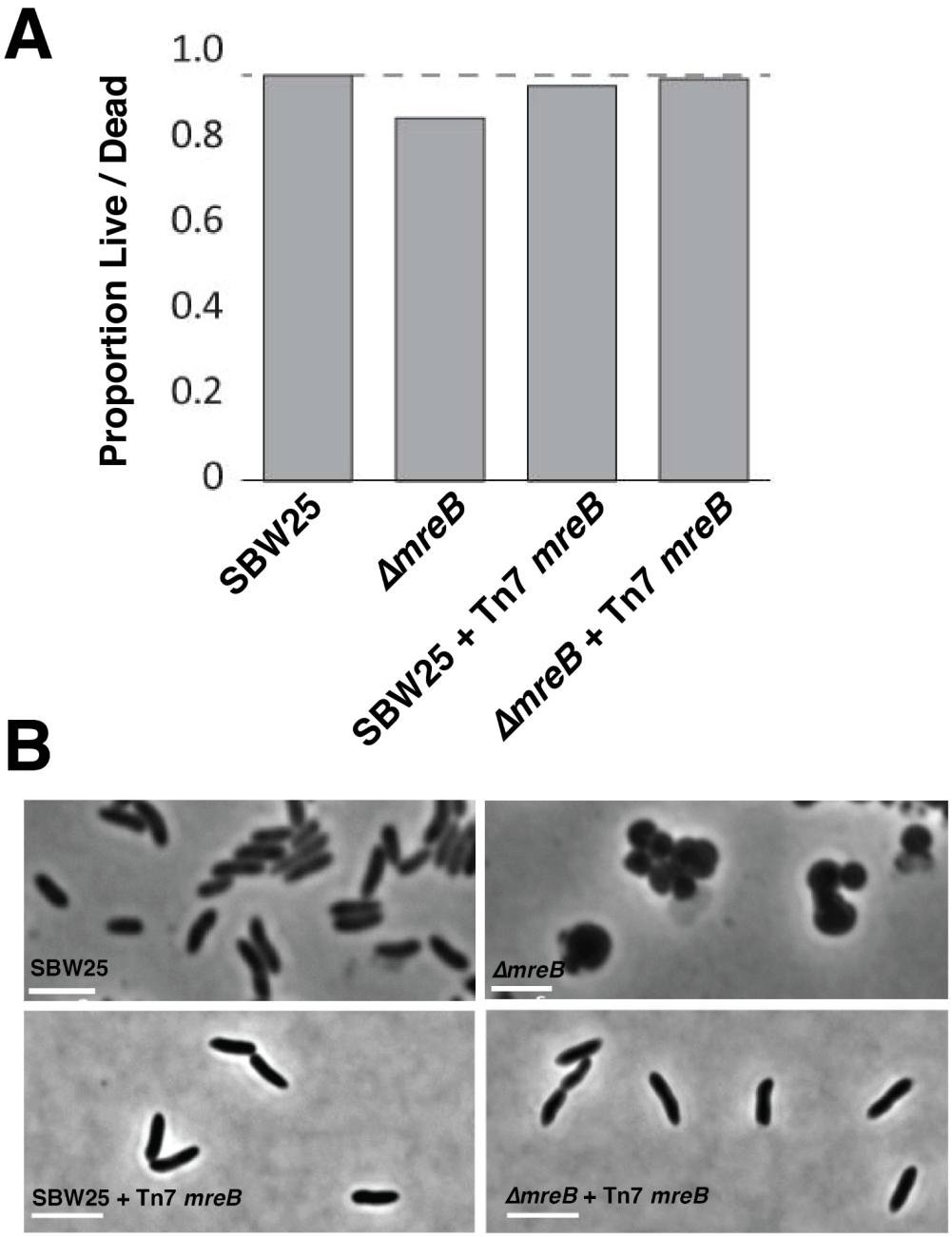

Supplementary Figure 4. Ancestral SBW25 and Δ*mreB* cells, with ectopically added MreB expressed from the *glmS* region of the chromosome. A) Viability of respective strains via live-dead cell staining. B) Phase contrast micrographs of SBW25, Δ*mreB* , SBW25 + Tn*7 mreB*, and Δ*mreB* + Tn*7 mreB*. Scale bars = 3 µm.

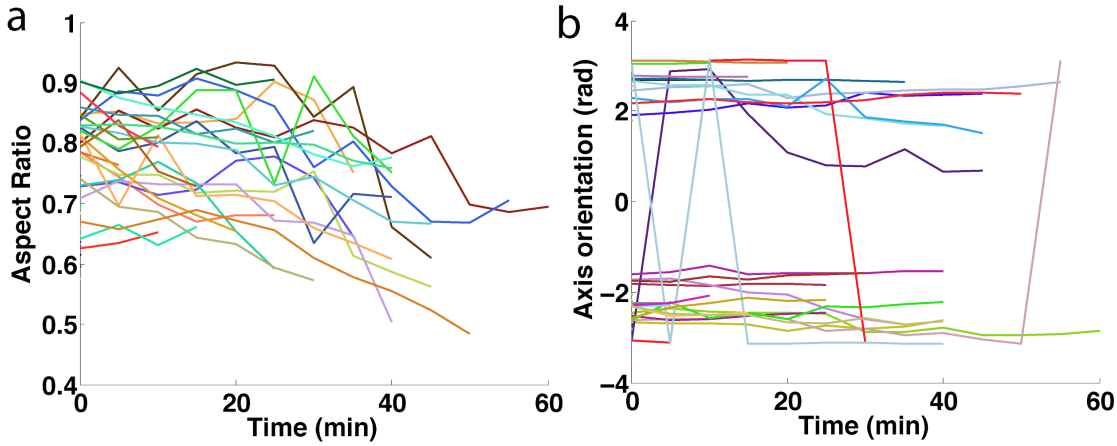

Supplementary Figure 5. a) Aspect ratio for Δ*mreB* cells. Aspect ratio is defined as the ratio between the short and the long axis of the cell mask fitted with an ellipse. The decrease of the aspect ratio indicates that the long axis grows faster than the short axis. b) Orientation of the elongation axis in Δ*mreB* cells is constant during the division. Angles are in radians. Sudden changes correspond to phase shift (angles are expressed within the interval [-π;π] with periodic boundaries). In a) and b), time traces are plotted from cell birth until septation.

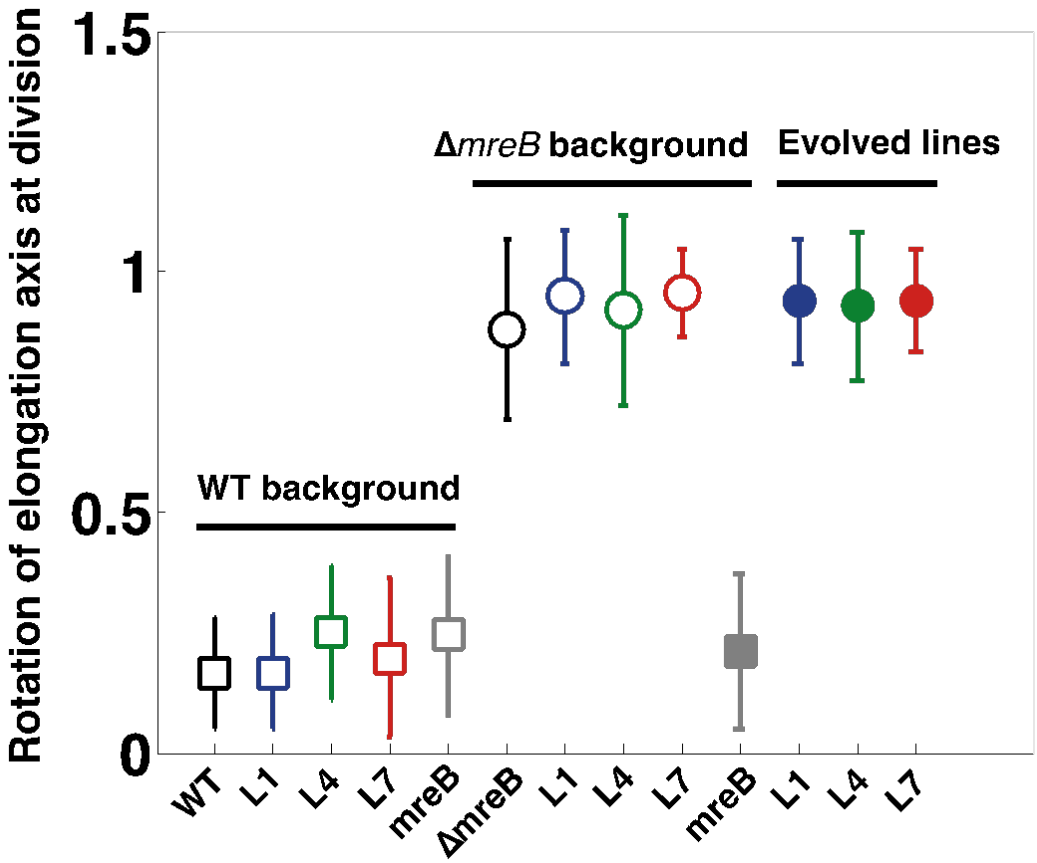

Supplementary Figure 6. From the angle, θ, between mother and sister cells, we compute the relative orientation between mother and daughter using |sin θ | in order to get average in populations. |sin θ |=0 means that mother and daughter cells are aligned, |sin θ |=1 means that they are perpendicular. Filled or open square data points represent rod-like cells and filled or open circles represent spherical cells. WT strains are labelled in black. Open squares and open circles represent the reconstruction of the different observed mutations in the WT and Δ*mreB* backgrounds, respectively. Filled circles represent the evolved lines where the mutations have been identified. Colors as in Fig 3; blue is Line 1 or PBP1a D484N, green is Line 4 or PBP1a T362P, red is Line 7, grey is ectopic *mreB* expression. Data are means and standard deviation (N_{WT} = 141; N_{L1_WT} = 78 ; N_{L4_WT} = 57; N_{L7_WT} = 110; N_{mreB_WT} = 54; $N_{\Delta mreB}$ = 154; $N_{L1_\Delta mreB}$ = 148; $N_{L4_\Delta mreB}$ = 164; $N_{L7_\Delta mreB}$ = 149; $N_{mreB_\Delta mreB}$ = 96; N_{L1} = 132; N_{L4} = 116; N_{L7} = 116).

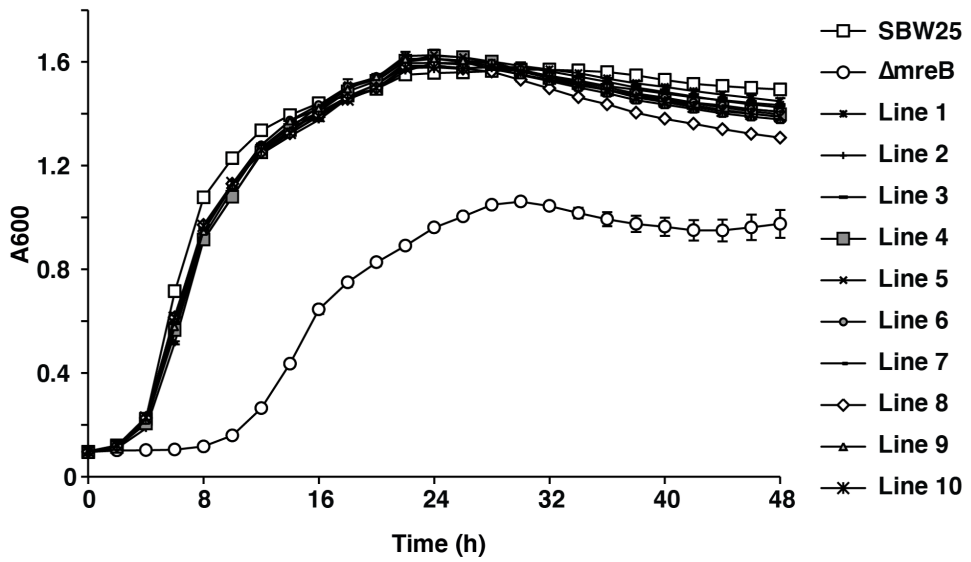

Supplementary Figure 7. Growth curves of evolved *ΔmreB* lineages after 1,000 generations of evolution. Ancestral SBW25 and Δ*mreB* are shown for comparison. NB: All growth curves were produced simultaneously as described in Figure Supp. 1, SBW25 (WT) and Δ*mreB* are shown for comparison.

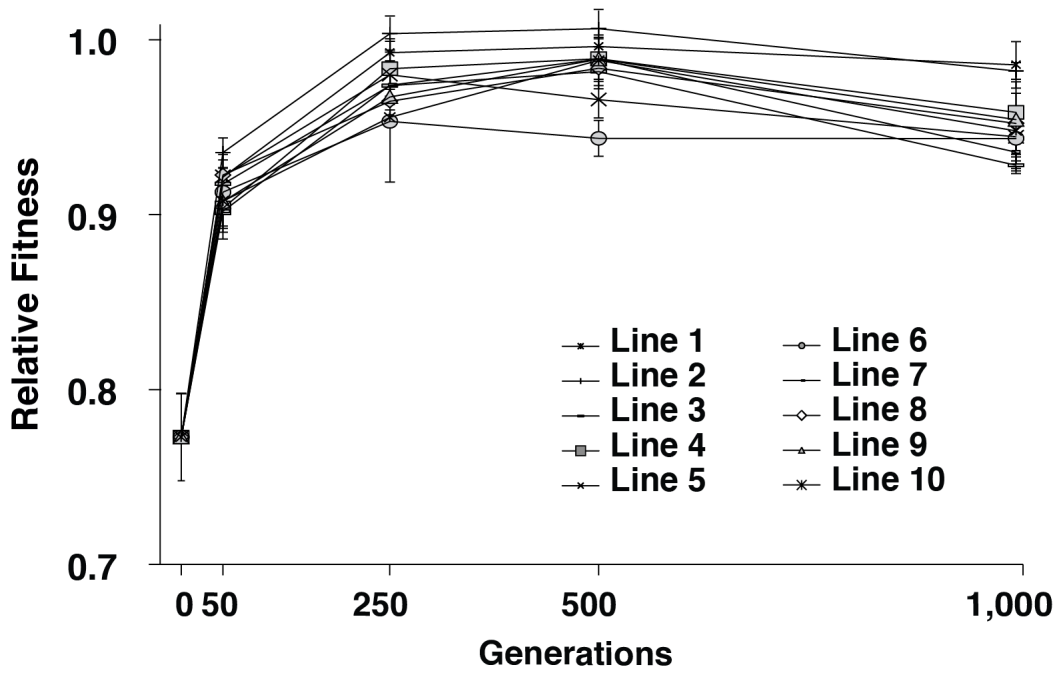

Supplementary Figure 8. Relative fitness of the evolved lines at distinct points during the 1,000 generations of evolution. Data are means and standard deviation of three biological replicates.

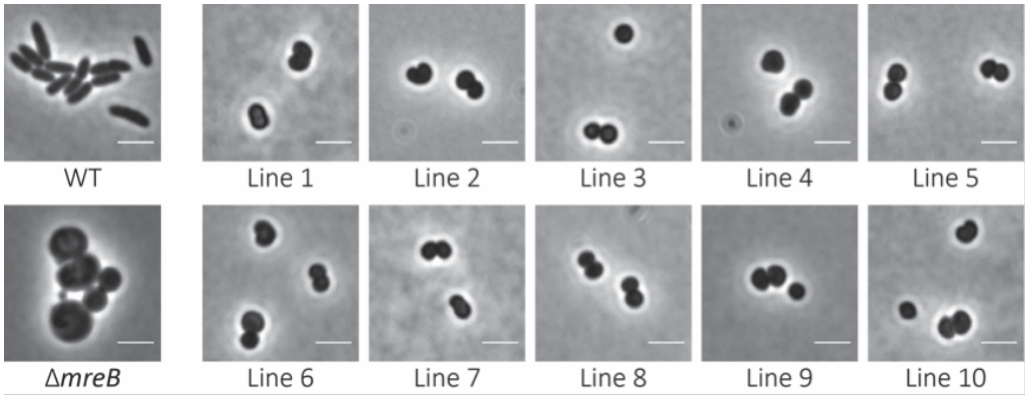

Supplementary Figure 9. Phase contrast images of the 10 independent evolved lines. Cells were harvested at log phase (OD_{600} = 0.4). Scale bars = 3 um.

```
Strep_agala|WP_000628365.1|      TRRNTVLQQMYQDKNISKKEYDQAVATPVTDGLKELKQKSTYPKYMDNYL-KQVISEVKQ   288
Escher_coli|CAP77843.1|          ARRNVVLSRMLDEGYITQQQFDQTRTEAINANYHAPEIAFSA-----PYLSEMVRQEMYN   282
Salmon_ent_Typhi|CAD08121.1|     ARRNVVLSRMLSEGYITQAQYDQARSEPIDANYHAPEIAFSA-----PYLSEMVRQEMYN   282
Pseudo_fluor|YP_002870086.1|     ERRDWILGRMYKLGKIDQAAYESAVAEPLNASYHVPTPEVNA-----PYIAEMARAEMVG   275
Pseudo_aeri_PA01|AAB39710.1|     ERRNWILERMLKLGFIDQQRYQAAVEEPINASYHVQTPELNA-----PYIAEMARAEMVG   274
Acineto_baum|ACJ59085.1|         ERRNWILGRMLQLGYISQTEYQKAVAEPINLNMPNRDLNNIH-----PYAGEMVRSELVK   250
Morax_cata|WP_003659066.1        ERRNWIIGRMHQEGFITASEKDAAIAEPMGLNIYQEKLDLNM-----PYVAEMVRSTLVD   288
                                  **: :: :* .   *     : :    :  .               *  : .   :

Strep_agala                      KTGKDIFTAGLKVYTNINTDAQKQLYDIYN----SDTYIAYPNNE--------------   329
Escher_coli                      RYGESAYEDGYRIYTTITRKVQQAAQQAVRNNVLDYDMRHGYRGPANVLWKVGESAWDNN   342
Salmon_ent_Typhi                 RYGESAYEDGYRIYTTITRKVQQAAQQAVRNNVLDYDMRHGYSGPANVLWKVGETAWDSK   342
Pseudo_fluor                     RYGSEAYTEGFRVTTTVPSNLQDIANEAVHSGLIDYDQRHGYRGPESRLPGKTLSAWTT-   334
Pseudo_aeri_PA01                 RYGSEAYTEGYKVITTVRSDLQNAASQSVRDGLIDYDQRHGYRGPETRLPGQTRDAWLK-   333
Acineto_baum                     HFGEQAIDSGYKVYTTINAKRQAIAEKAVQDGLEAYDRRHGWRGAEAHD---------K-   300
Morax_cata                       RYGEAVMDSGWRVQTTINSSSQLAANAALVGGLRDYDRRHGWRGVEAES---------G-   338
                                 : *.     * :: *.:  . *             *   .: .
                                                        Line 4 T363P
Strep_agala                      ------------------------------------------------------------   329
Escher_coli                      KITDTLKALPTYGPLLPAAVTSANPQEATAMLADGSTVVLSMEGVRWARPYRSDTQQGPT   402
Salmon_ent_Typhi                 KITDTLKALPTYGPLLPAVVTSANPQEATAALADGTSVSLHMEGMRWARPYRSDTQQGPT   402
Pseudo_fluor                     ----ELGKQRPISGLEPAIVTQVKKDGVQVLTRTGE-AHVAWDSMKWARPFLNTNSMGAM   389
Pseudo_aeri_PA01                 ----HLGQQRSIGGLEPAIVTQVEKSGIMVMTRDGKEEAVTWDSMKWARPFLSNNSMGPM   389
Acineto_baum                     ----PLSEFRAYANTYPAQVTKVNSSSFEALMQDGSTVTVQWSGMSWARPYRNANSVGAA   356
Morax_cata                       ----SLEGRKNFDHIYPAKVTKVHNQSFEAKLQSGETVTIGWSGMNWARRYYDANRVGGG   394

Strep_agala                      --------------------------------LQIASTIMDATNGKVIAQLGGRHQNEN   356
Escher_coli                      PRKVTDVLQTGQQIWVRQ---VGDAWWLAQVPEVNSALVSINPQNGAVMALVGGFDFNQS   459
Salmon_ent_Typhi                 PRKVTDVVQTGQQIWVRQ---VDNDWWLAQVPEVNSALVSLNPQTGAVLALVGGFDFNQS   459
Pseudo_fluor                     PKQPSDVAQVGDLIRVQRQ--KDDSLKFSQVPLAQGALVSLDPQNGAIRALVGGFAFEQS   447
Pseudo_aeri_PA01                 PRQPADVAQAGDQIRVQRQ--EDGTLRFVQIPAAQSALISLDPKDGAIRSLVGGFSFEQS   447
Acineto_baum                     PSRASQIVKVKDIVRLRP-NEAKTAWSLVQVPKVQGQLIAINPNDGSIEAIVGGYNFYQS   415
Morax_cata                       YSNAHQMVKVGNIVRISPINEAKTAWRMESIPKVQGALVSLDPENGALRAVVGGFHFNHS   454
                                                                  :     ::   * : : :**    ..

Strep_agala                      ISFGTNQSVLTDRDWGSTMKPISAYAPAIDSGVYNSTGQSLNDSVYYWPGTS---TQLYD   413
Escher_coli                      ---KFNRATQALRQVGSNIKPF-LYTAAMDKG-LTLASMLNDVPISRWDAGAGSDWQPKN   514
Salmon_ent_Typhi                 ---KFNRATQALRQVGSNIKPF-LYTAAMDKG-LTLASMLNDVPISRWDAGAGSDWRPKN   514
Pseudo_fluor                     ---NYNRATQAKRQPGSSFKPF-IYSAALDNG-YTAASLVNDAPIVFVDEYLDKVWRPKN   502
Pseudo_aeri_PA01                 ---NYNRAIQAKRQPGSSFKPF-IYSAALDNG-FTAASLVNDAPIVFVDEYLDKVWRPKN   502
Acineto_baum                     ---KFNRALQGWRQPGSTIKPF-LYALALERG-MTPYSMVNDSPITI------GKWTPKN   464
Morax_cata                       ---KFNRAIQGYRQPGSIIKPF-IFAAALESGQYTPDSLISDAAIRV------GRWQPKN   504
                                      *::    *: ** :**:  :: *:: *  .  .   :  :              :
                                                                   Line 1 D484N
Strep_agala                      WDRQYMGWMSMQTAIQQSRNVPAVRALEAAGLDEAKSFLEKLGIY-YPEMNYSNAISSNN   472
Escher_coli                      SPPQYAGPIRLRQGLGQSKNVVMVRAMRAMGVDYAAEYLQRF-GFPAQNIVHTESL----   569
Salmon_ent_Typhi                 SPPQYAGPIRLRQGLGQSKNVVMVRAMRAMGVDYAAEYLQRF-GFPAQNIVHTESL----   569
Pseudo_fluor                     DTNTFLGPIRIREALYKSRNLVSIRLLQAMGVGKTIDYMTRF-GFAKSDLPPNLSL----   557
Pseudo_aeri_PA01                 DTNTFLGPIPLREALYKSRNMVSIRVLQGLGIERAISYITKF-GFQRDELPRNFSL----   557
Acineto_baum                     SDGRYLGMIPLRRALYLSRNTVSVRLLQTVGIERTRQLFMDF-GLQEDQIPRNYTI----   519
Morax_cata                       ADGRYTGDMTLRRALTLSRNTPAIRLLRSAGVDESRHLMNAMGGLEIERMPSTLAL----   560
                                     : * : :: .:  *:*   :* :.  *:  :   :  :       :  . ::
```

Supplementary Figure 10. A Clustal Omega sequence alignment of a segment of Pbp1A amino acid sequences from seven bacterial species, including *A. baumannii*, which was used for the construction of the protein model showing the location of the evolved line mutations. NB: *Streptococcus* does not contain the OB/ODD domain. Regions of interest containing the evolved Line 1 and 4 mutations are shown. Mutated residues are in bold. The mutations are shaded in red and green respectively and labeled accordingly. Strictly conserved residues are labelled below the alignment with asterisks.

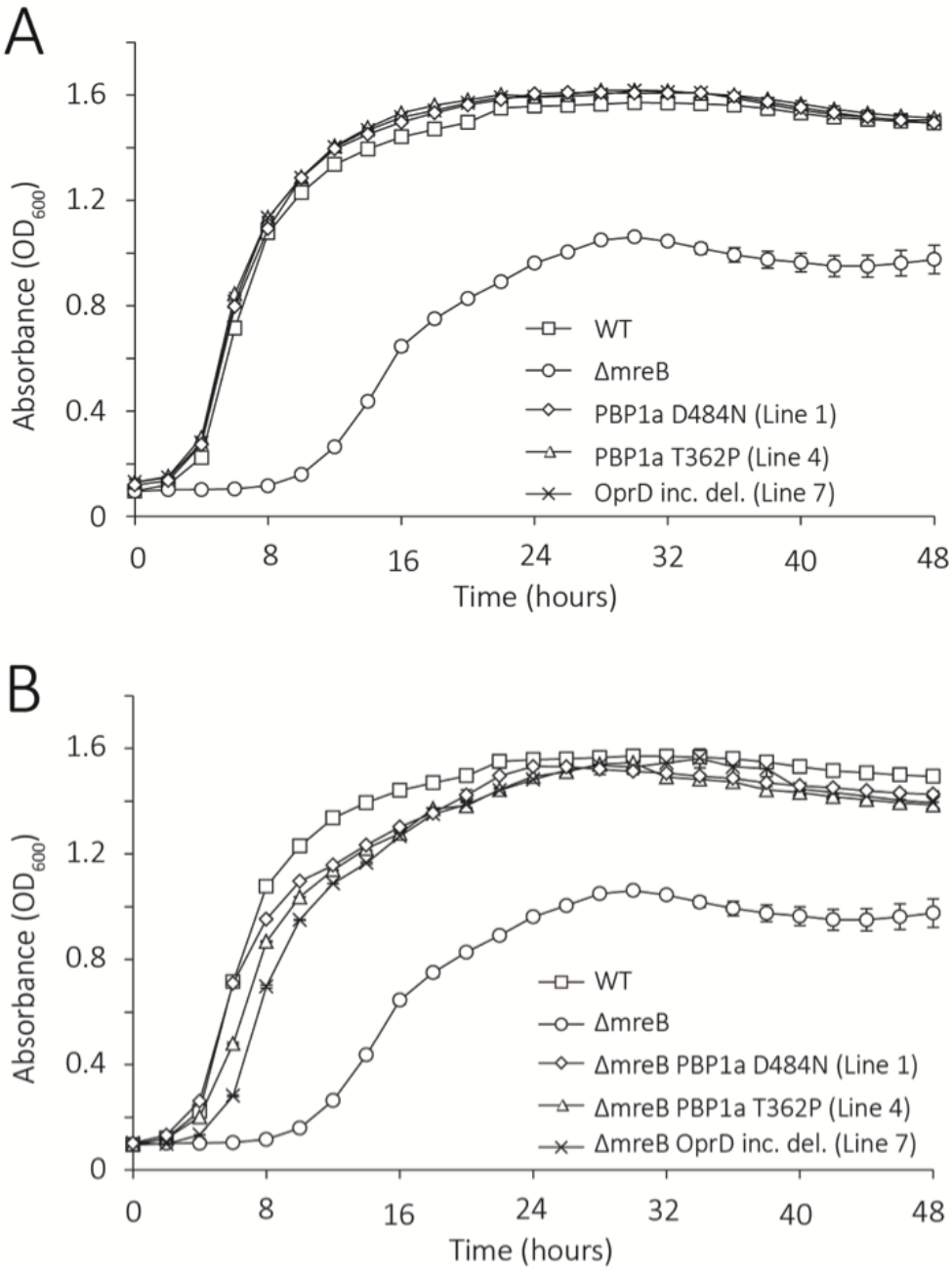

Supplementary Figure 11. Growth curves of the reconstructions in A) SBW25 and B) Δ*mreB* backgrounds. NB: All growth curves were produced simultaneously as described in Fig Supp. 1. Ancestral SBW25 (WT) and Δ*mreB* are shown for comparison.

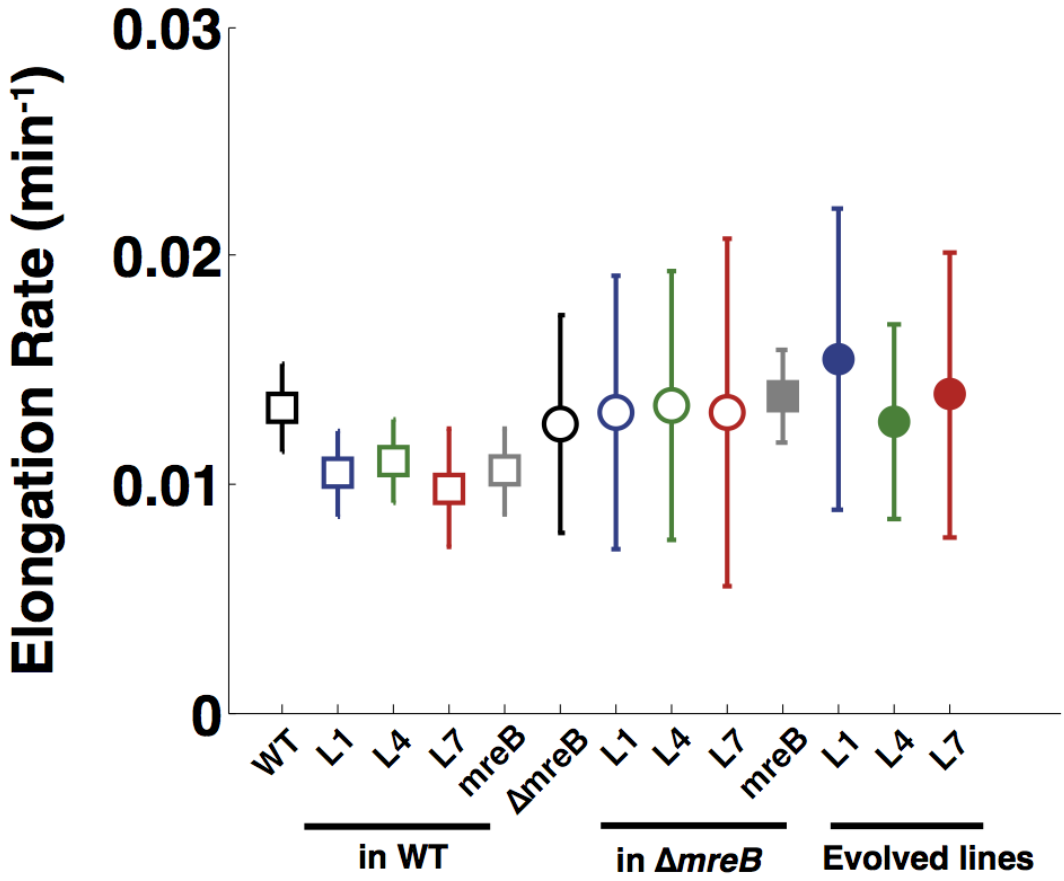

Supplementary Figure 12. Elongation rate measures the rate, r, at which cell volume increases $V(t)=V_0e^{rt}$. Filled or open square data points represent rod-like cells and filled or open circles represent spherical cells. Ancestral SBW25 (WT) strains are labelled in black. Open squares and open circles represent the reconstruction of the different observed mutations in the WT and Δ*mreB* backgrounds, respectively. Filled circles represent the evolved lines where the mutations have been identified. Colors as in Fig 3; blue is Line 1 or PBP1a D484N, green is Line 4 or PBP1a T362P, red is Line 7, grey is ectopic *mreB* expression. Error bars represent standard deviations. (N_{WT} = 94; N_{L1_WT} = 52 ; N_{L4_WT} = 38; N_{L7_WT} = 72; N_{mreB_WT} = 36; $N_{\Delta mreB}$ = 99; $N_{L1_\Delta mreB}$ = 92; $N_{L4_\Delta mreB}$ = 102; $N_{L7_\Delta mreB}$ = 96; $N_{mreB_\Delta mreB}$ = 64; N_{L1} = 88; N_{L4} = 74; N_{L7} = 76)

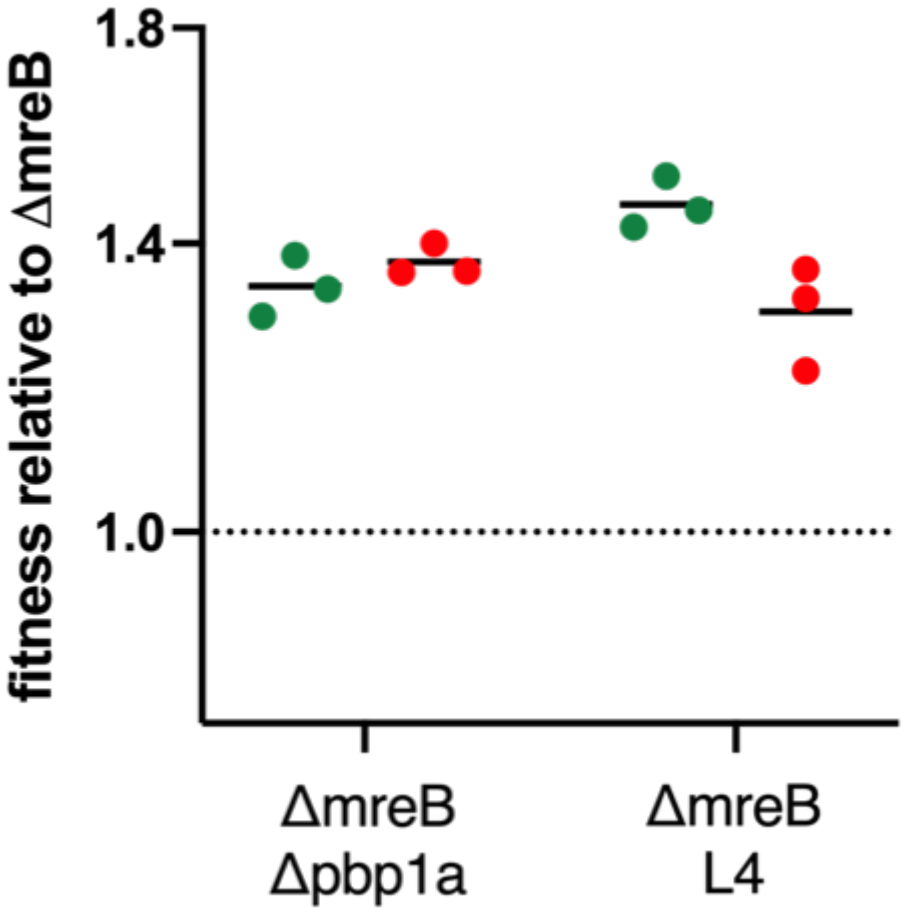

Supplementary Figure 13. Fitness of SBW25 Δ*mreB* Δ*pbp1A* and Δ*mreB pbp1A* (T362P) relative to SBW25 Δ*mreB* and. Each genotype was marked separately with green and red fluorescent protein allowing reciprocal fitness measures to control for any marker effect. Data were collected by flow cytometry.

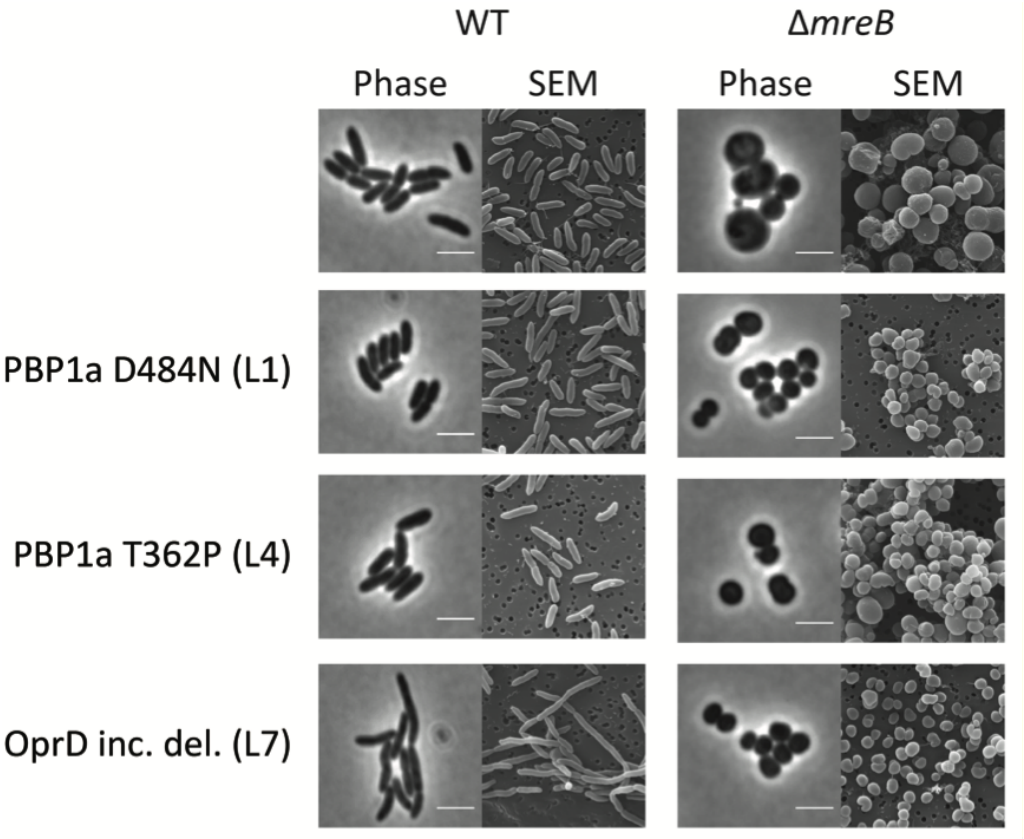

Supplementary Figure 14. Cell morphologies. Phase contrast and SEM images of reconstruction strains. Reconstructions in either the SBW25 or the Δ*mreB* background are depicted. SBW25 (WT) and Δ*mreB* are shown for comparison. Scale bars = 3 um.

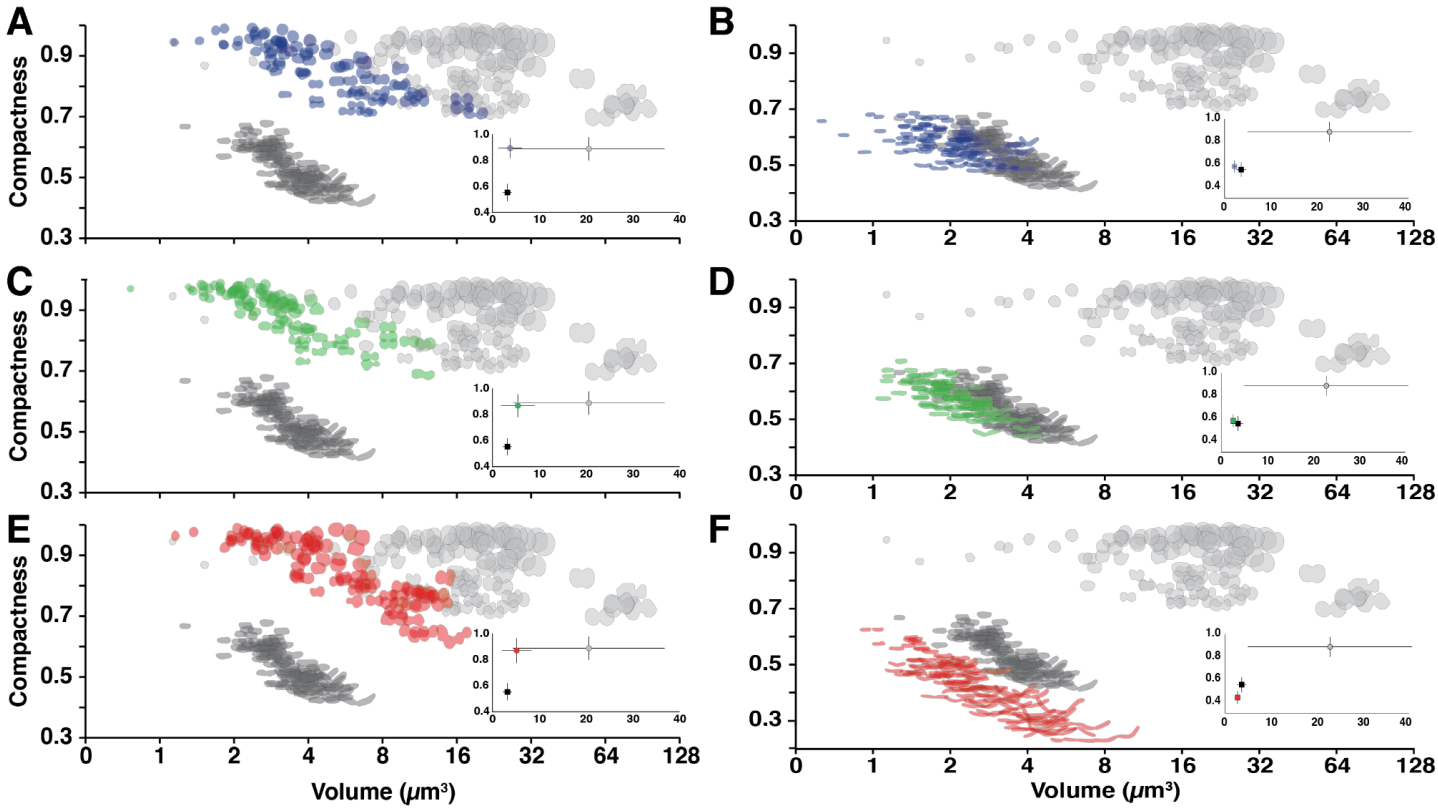

Supplementary Figure 15. The cell morphologies and relationship between cell shape and estimated volume (V_e) represented using compactness as in Fig 1B of mutation reconstructions. Cell shape for each mutation of interest in A) the Line 1 or PBP1a D484N in Δ*mreB* and B) in SBW25. C) The Line 4 or PBP1a T362P in Δ*mreB* and D) in SBW25. E) The Line 7 PFLU4921-4925 Δ5399934-5403214 in Δ*mreB* and F) in SBW25. All populations are shown alongside the Δ*mreB* and SBW25 morphologies for reference. Colours are as Fig 2. Insets as in Fig 2B reflecting the Stfor the mutant populations. One hundred representative cells from each population are shown.

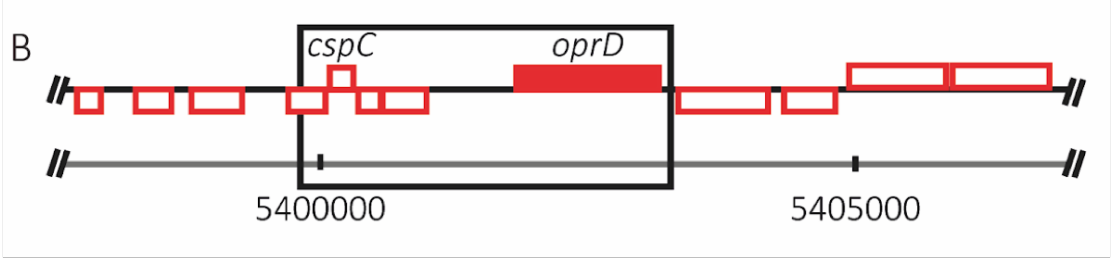

Supplementary Figure 16. Genome map of the *oprD* inclusive deletion, (PFLU4921-4925 Δ5399934-5403214) and surrounding region. Genes with function calls are noted.

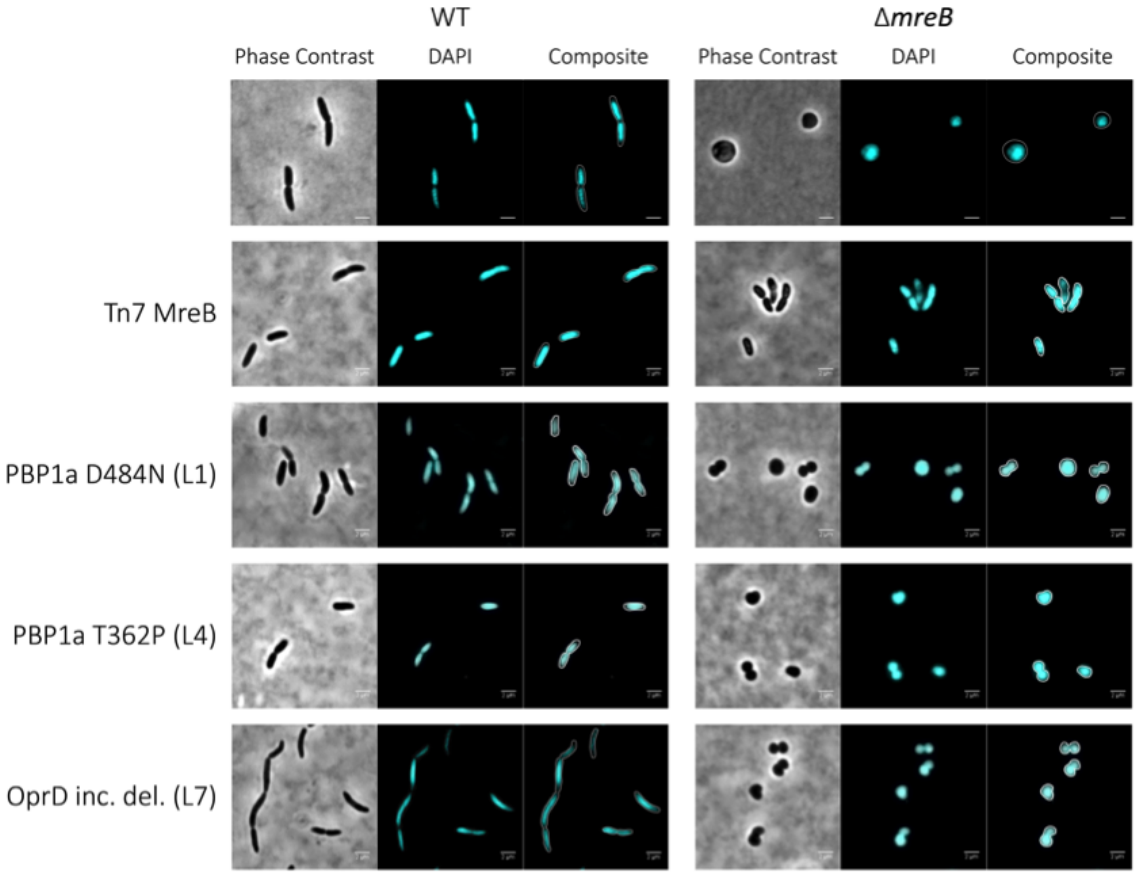

Supplementary Figure 17. Reconstruction of Line 1, 4 and 7 mutations in ancestral SBW25 (WT) and SBW25 Δ*mreB* background stained with DAPI. SBW25 and Δ*mreB* cells shown for comparison. DNA segregation defects appear to be common at septation in this population. Scale bars = 2 um.

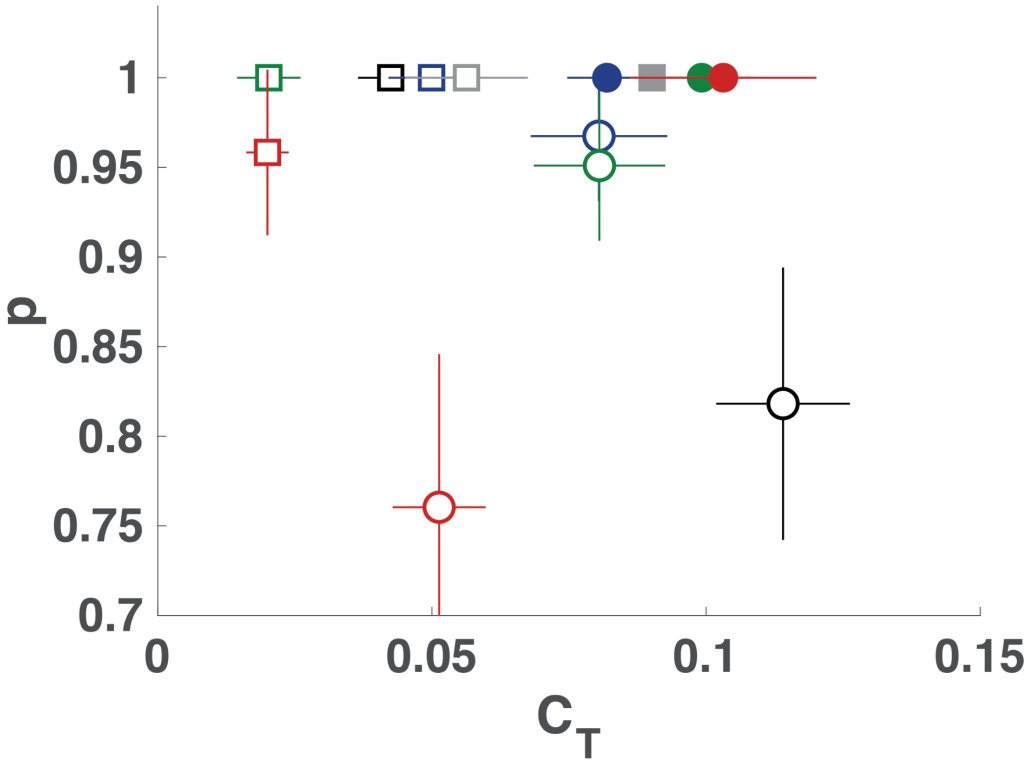

Supplementary Figure 18. The probability *p* to pass to the next generation as a function of division time asymmetry C_T. Division time asymmetry is measured as the relative time elapsed between cell birth and division. Error bars represent standard errors (N_{WT} = 94; N_{L1_WT} = 52 ; N_{L4_WT} = 38; N_{L7_WT} = 72; N_{mreB_WT} = 36; $N_{\Delta mreB}$ = 99; $N_{L1_\Delta mreB}$ = 92; $N_{L4_\Delta mreB}$ = 102; $N_{L7_\Delta mreB}$ = 96; $N_{mreB_\Delta mreB}$ = 64; N_{L1} = 88; N_{L4} = 74; N_{L7} = 76). Filled or open square data points represent rod-like cells and filled or open circles represent spherical cells. Ancestral SBW25 genotypes are labelled in black. Open squares and open circles represent the reconstruction of the different observed mutations in the ancestral and Δ*mreB* backgrounds, respectively. Filled circles represent the evolved lines where the mutations have been identified. Colors as in Fig 3; blue is Line 1 or PBP1a D484N, green is Line 4 or PBP1a T362P, red is Line 7, grey is ectopic *mreB* expression.

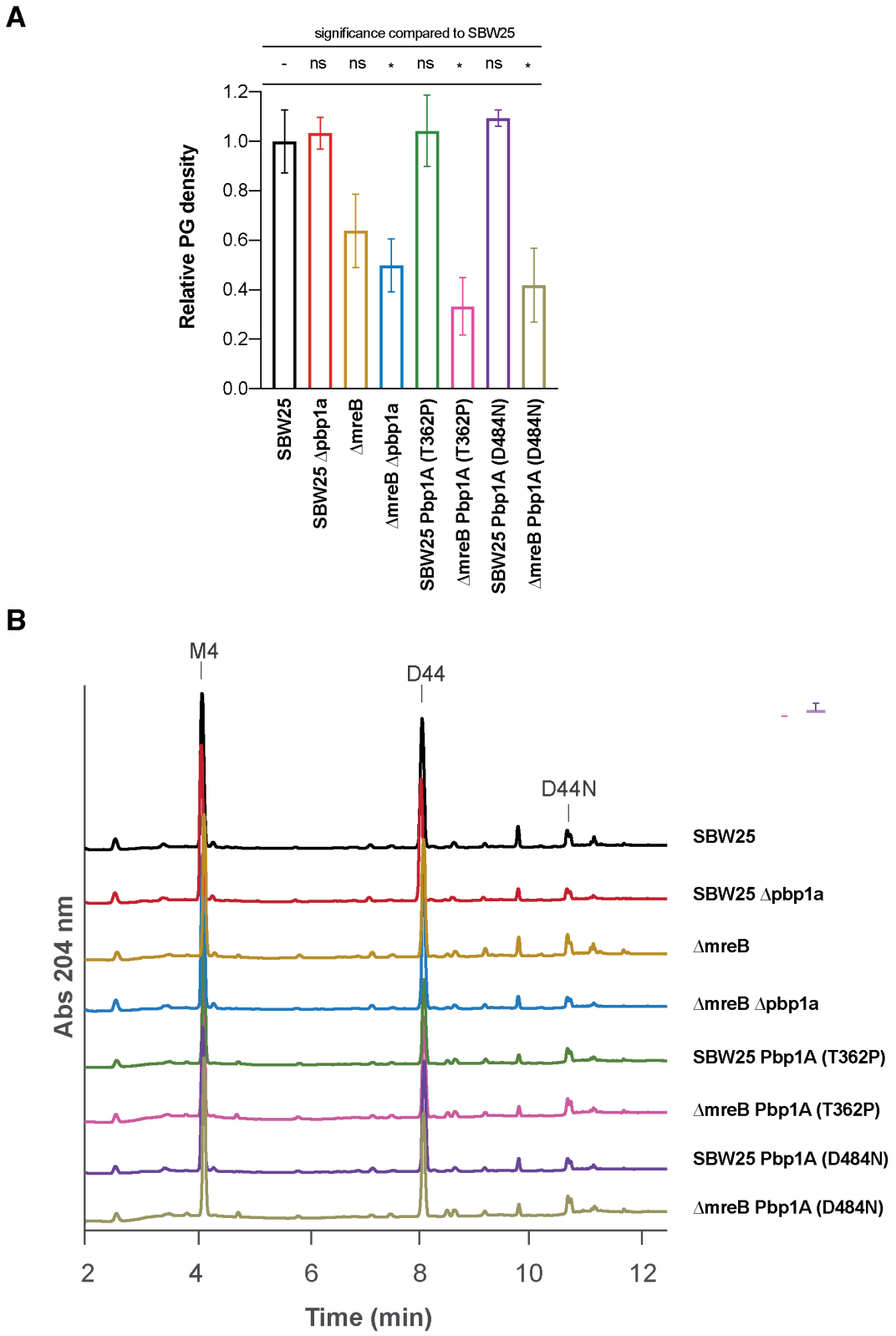

Supplementary Figure 19. A. Peptidoglycan analysis showing the relative PG density of different *P. fluorescens* strains relative to SBW25 (wild type). Error bars (SD) are the result of 3 biological replicates. ANOVA revealed a highly significant difference among means [$F_{7,16} = 16.74$, $p < 0.001$] with Dunnett's post-hoc test adjusted for multiple comparisons

showing that three genotypes (*) differ significantly ($p < 0.05$) from SBW25. B. UPLC spectra of the peptidoglycan profiles of the different *P. fluorescens* strains. Major muropeptide peaks were labelled as M4 (monomer disaccharide tetrapeptide), D44 (dimer disaccharide tetra-tetrapeptide) and D44N (anhydrous dimer disaccharide tetra-tetrapeptide).

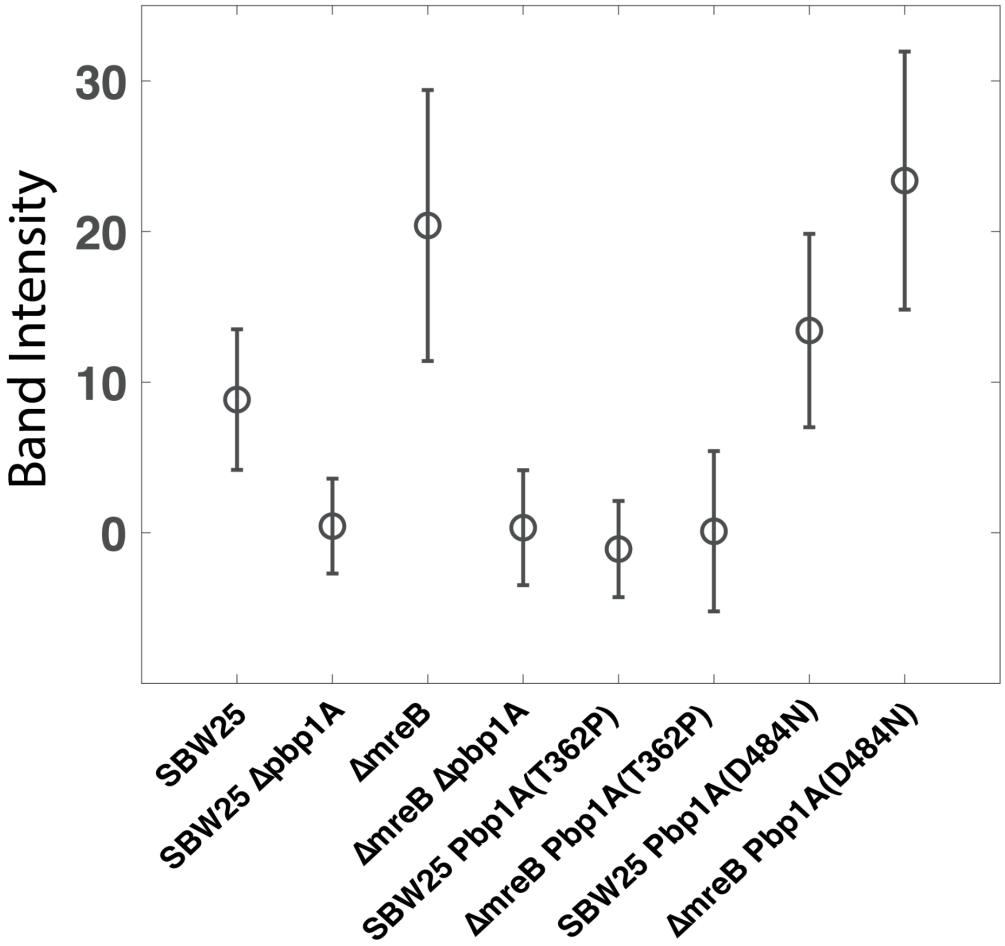

Supplementary Figure 20. Quantification of band intensity corresponding to PBP1A TPase activity as presented in the gel shown in Fig 4B. Band intensity was measured from the raw image of the gel. For each condition, we measured the mean background level and subtracted the mean grey level of the band measured in ROIs of the same size.

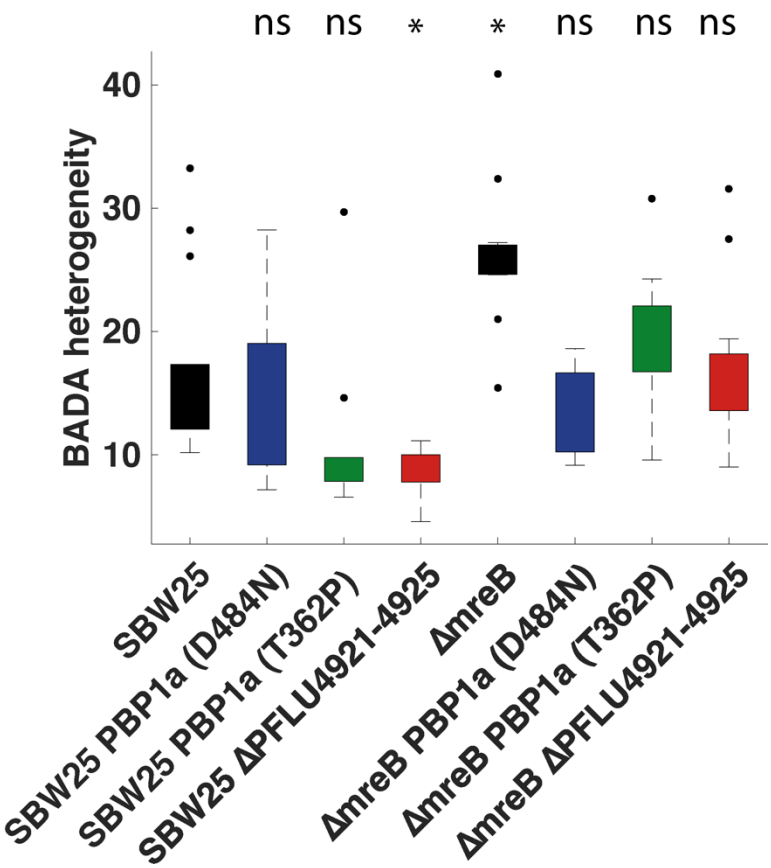

Supplementary Figure 21. Quantification of heterogeneity in cell wall synthesis as determined by BADA-labelling (see Fig 4C). Data are standard deviations divided by the square root of the mean pixel intensity (y-axis) of between 10 and 14 cells for each cell lineage. To rule out possible artefacts associated with variation of the mean intensity, we calculated BADA heterogeneity as the ratio of the standard deviation divided by the square root of the mean. ANOVA revealed a highly significant difference among means [$F_{7,89} = 9.97$, $p < 0.0001$] with Dunnett's post-hoc test adjusted for multiple comparisons showing that SBW25 Δ*mreB* and SBW25 ΔPFLU4921-4925 are significantly different (*) from SBW25 ($p < 0.05$).